
UNIVERSITY OF PADOVA

DEPARTMENT OF INFORMATION ENGINEERING

*Master's Level Degree in Bioengineering*

# Diffusion tensor imaging tractography of the facial nerve for the pre-surgical plan in patients with vestibular schwannoma

*Candidate:*
Manuela Moretto

*Supervisor:*
Prof. Alessandra Bertoldo

*Cosupervisors:*
Dr. Sabrina Brigadoi
Dr. Marco Castellaro

Academic year 2017/2018

To my love, Andrea

# Contents

# Abstract

Patients with vestibular schwannoma (VS) may experience facial nerve (FN) damage after surgery, leading to possible facial paralysis. This is because the FN can be dislocated by the VS and therefore its location is a priori unknown to the surgeon. The aim of this thesis is to evaluate the feasibility to use DTI fiber tracking algorithms for the preoperative determination of FN course in patients with VS and to optimize the DTI sequence to decrease the total acquisition time and improve FN reconstruction.
In this thesis, starting from an accurate evaluation of the state of the art, a multi-shell DTI acquisition protocol was optimized and it was included in the standard presurgical MR protocol. The presurgical MR data of five patients with VS were analyzed. Both deterministic (FACT) and probabilistic (SD STREAM and iFOD2) fiber tracking algorithms were applied for the reconstruction of FN course. The acquired multi-shell DTI data were then subsampled in four subprotocols: three mono-shell DTI protocols and one with half diffusion directions with respect to the original one. The performance of these reduced protocols was compared with that of the total protocol, to evaluate the feasibility to reconstruct a reliable facial nerve course with a shorter acquisition time for the patient.
The qualitative validation of the results was carried out with a team of experienced physicians, comparing the position of the FN with respect to the tumor location found in-vivo during the surgery with that obtained with iFOD2 algorithm applied to the total acquisition protocol. The first quantitative analysis consisted in comparing the total and reduced protocols by assigning a score related to the reliability of the results of the tractography for the two probabilistic tracking methods and acquisition protocols. Four common diffusion indices were also computed for each patient and protocols for both probabilistic tractography algorithms, with the aim to evaluate a possible relationship between facial nerve integrity and its functionality before the surgery.
The reconstructions of FN showed that the FACT algorithm failed to generate any streamline in any of the patients. The qualitative validation results showed that in three of the five patients, the FN reconstruction confirmed the nerve course that was observed intraoperatively. For the other two patients the reconstruction did not show clear results. These two patients presented a very challenging and particular position of the FN. Although not completely faithful to the intraoperative findings, the reconstructed FN in these two patients provided important and useful information that could have helped surgeons to better plan the oper-

ation, if known in advance. The scores resulting from the comparison between methods and protocols suggested that the iFOD2 algorithm, applied to the total protocol, is the most suitable for FN reconstruction. It is followed by the SD STREAM algorithm, applied to the total protocol, which could be used as a supplementary reconstruction method to help to achieve a greater reliability of the results obtained with the iFOD2 algorithm. These results also showed that the total protocol can not be reduced if physiologically reliable results want to be obtained. Therefore, the total protocol seems to have the minimum requirements for a reliable reconstruction of the FN in patients with VS. The analysis on the diffusion indexes did not give faithful information on the nerve integrity, although offering interesting results in one of the difficult patients.

# Chapter 1

# Introduction

Vestibular schwannomas are intracranial tumours that affect 1% of the population. Most of these tumors are treated surgically with the aim to excise the tumor and preserve the functions of the nerves located nearby. One of these nerves is the facial nerve, whose main function is to control all the muscles responsible for facial expression. However, 20% of the patients undergoing this type of surgery still experience a partial or total damage to the facial nerve [1]. The main reason is that the facial nerve can be dislocated by the tumor and therefore its location is a priori unknown to the surgeon. Diffusion tensor imaging (DTI) tractography has be shown to have the potential to predict the location of the cranial nerves, including the facial nerve (FN). Employing DTI tractography to predict FN location nearby the tumor is however not an easy task, since several nerves are present in the tumor area, very close to each other (see Figure 1.1). Previous studies indeed failed to reach a 100% accuracy in the prediction of the FN location. The aim of this thesis is to optimize the DTI acquisition protocol and the pipeline for DTI tractography analysis for the preoperative determination of the facial nerve course in patients with vestibular schwannomas. The results of this analysis will be compared with intraoperative findings, thanks to a team work that has involved several doctors of the University Hospital of Padova.

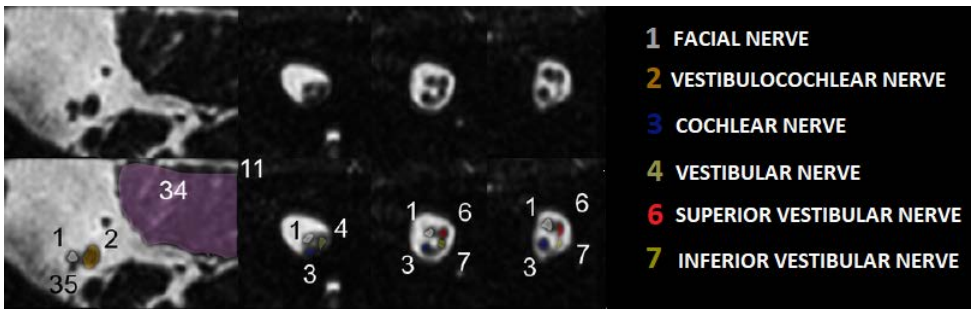


Figure 1.1: Sagittal series of a high-resolution T2-weighted MR image showing the sections of the internal auditory canal from medial to lateral part. The colored numbers distinguish the main nerves that result to be very close one to each other. Adapted from [2].

## 1.1 Vestibular schwannoma

### 1.1.1 Anatomy

Vestibular schwannomas (acoustic neuromas) account for about 5% of intracranial tumors and more than 90% of cerebellopontine angle (CPA) tumors. The tumor originates from an overproduction of Schwann cells, which normally enclose the nerve fibers to help support and isolate nerves. These tumors are benign and usually slow-growing. They originate in the internal auditory canal, producing symptoms related to the compression of the nerve in the narrow boundaries of the canal [3]. As the tumor grows, it juts out from the internal auditory meatus and it can affect both the face sensation nerve (the trigeminal nerve), causing facial numbness, and the facial nerve (for the muscles of the face) causing facial weakness or paralysis on the side of the face ipsilateral to the tumor. If the tumor becomes large, it will eventually press against nearby brain structures (such as the brainstem and the cerebellum), becoming life-threatening. As the vestibular schwannoma grows, it affects the hearing and balance nerves as well, usually causing unilateral (one-sided) or asymmetric hearing loss, tinnitus (ringing in the ear), and dizziness/loss of balance [4]. Figure 1.2 depicts the composition of the ear, including the outer ear, middle ear, and inner ear. From the visible part of the outer ear that resides outside of the head, the auditory canal leads to the ear drum and the middle ear. The middle ear is made up of three bones: malleus, incus and stapes, that are behind the ear drum. Further inside and past the middle ear is the cochlea, a snail shaped organ. The cochlear nerve links the cochlea with the brain. The vestibular nerve is located outside the cochlea. The facial nerve runs parallel to the cochlear nerve towards the brain. Further inside the skull a vestibular schwannoma, which is enveloped by the auditory and facial nerves, is displayed.

### 1.1.2 Diagnosis

The first and most common symptoms of an acoustic neuroma are: unilateral or asymmetric hearing loss, tinnitus and loss of balance or dizziness. Unfortunately, early detection of the tumor is sometimes difficult because the symptoms may be subtle and may not appear at the starting stages of growth. Furthermore, hearing loss, dizziness, and tinnitus are common symptoms of many middle and inner ear problems. Once the symptoms appear, an accurate ear examination and hearing and balance testing (audiogram, electronystagmography, auditory brainstem responses) are therefore essential for proper diagnosis. Magnetic resonance imaging (MRI) scans are crucial for the early detection of a vestibular schwannoma and are helpful in determining the location and size of a tumor and in planning its microsurgical removal [4].

### 1.1.3 Therapy

Early diagnosis of a vestibular schwannoma is fundamental to prevent its severe consequences. There are three main options for managing an acoustic neuroma:

1. surgical removal: the specific type of operation depends on the size of the tumor and the level of hearing in the injured ear. The goal of surgery is to remove the tumor, preserve the facial nerve to prevent facial paralysis and preserve hearing when possible. If the tumor is small, hearing may be preserved and accompanying symptoms may improve after its removal. As the tumor grows larger, surgical removal becomes more complicated because the tumor may have damaged the nerves that control facial movement, hearing, and balance and may also have affected other structures close to the brain. The removal of tumors affecting the hearing, balance, or facial nerves can sometimes worsen the patient's symptoms because these nerves may be injured during tumor removal [4]. Figure 1.3 shows an example of vestibular schwannoma during a surgery for its removal.

2. radiation: radiosurgery, such as Gamma Knife radiosurgery, may be adopted to reduce the size or limit the growth of the tumor. It consists of a delivery of a precise dose of gamma rays on the area occupied by the tumor. This technique does not damage the surrounding tissue and it does not make any incision. Using imaging scans, physicians pinpoint the tumor and then plan the direction of the radiation beams [5]. Radiation therapy is sometimes the preferred option for elderly patients, patients in poor medical conditions, patients with bilateral vestibular schwannoma (tumor affecting both ears), or patients whose tumor is affecting their only hearing ear. Risks of radiosurgery include hearing loss, ringing in the ear, facial weakness, facial numbness, balance problems and treatment failure that leads a progressive growth of the tumor.

3. observation: when the tumor is small or it grows slowly and causes few or no signs or symptoms, it may be reasonable to monitor the tumor especially if the patient is an older adult or otherwise not a good candidate for more-aggressive treatments. MR scans and hearing tests are used to carefully monitor the growth of the tumor [4].

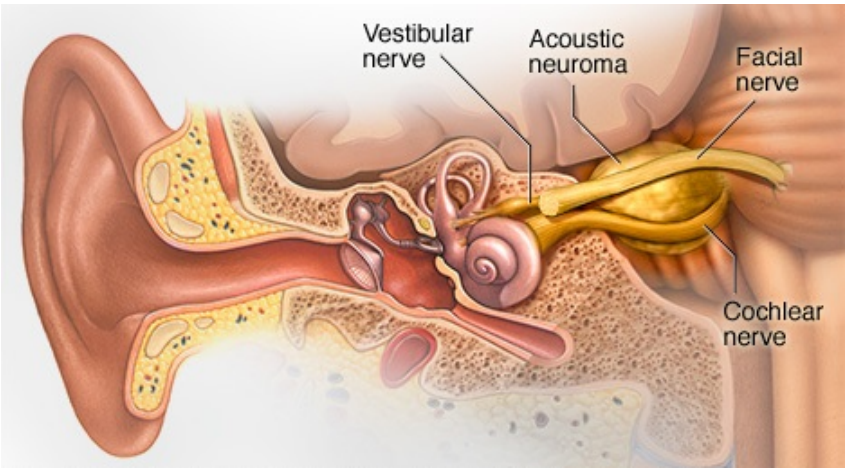


Figure 1.2: Illustration showing the different parts of the ear: inner ear, middle ear, outer ear. The auditory canal starts from the outer ear and leads to the ear drum and the middle ear. The middle ear consists of three bones located behind the ear drum: malleus, incus and stapes. Further inside we find the cochlea, a snail shaped organ pasting the middle ear, from which the cochlear nerve originates. Outside the cochlea there is the vestibular nerve, from which vestibular schwannoma originates. Facial nerve runs parallel to the cochlear nerve toward the brain. Further inside the skull there is a acoustic neuroma wrapped around the vestibular nerve and dislocating the facial nerve. Taken from [6].

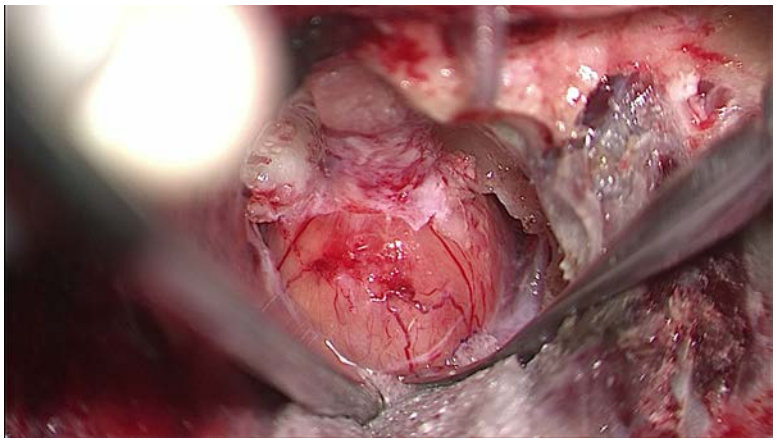

Figure 1.3: Surgical view of a vestibular schwannoma during a translabyrinthine removal.

## 1.2 Diffusion tensor imaging (DTI)

During the twentieth century many magnetic resonance imaging (MRI) techniques were developed and among these, diffusion tensor imaging (DTI) is one of the most powerful, since it allows to study the alterations of the microstructure in several neurological disorders in a non-invasive way [7]. The main advantage of diffusion tensor imaging consists in its ability to capture the information regarding the diffusion motion of water molecules at the microscopic level, which is otherwise not feasible with other conventional MR techniques. Within a tissue, water molecules have a random motion and the way they move is influenced by several factors such as restrictions due to cell membranes, cytoskeleton and macromolecules. Therefore, by studying how these factors contribute to the overall diffusional process, it may be possible to obtain helpful information about the biological microstructure and eventually about its alterations. Diffusion images are obtained by increasing the attenuation with the application of additional gradients. Therefore, this process exploits a contrast mechanism different than that in relaxation-weighted MRI. The maps of the signal intensity S, obtained through this mechanism, are called diffusion-weighted images (DWI).
Neural regions are connected through axons that function as transmission lines between these regions. Since water molecules tend to diffuse more freely along the direction of the fiber, if we can quantify the orientational preference of diffusion, it may be possible to relate it to the axonal orientations [8]. The extent of the diffusive phenomenon typical of neural fibers is characterized numerically through diffusion imaging, by determining for each voxel the so-called diffusion ellipsoid, mathematically described by a diffusion tensor. Starting from this tensor, one can derive the diffusion indices, introduced in detail in subsection 1.2.5, which quantify the type of diffusional process that affects the brain regions. The 3D representation of the structure of the fibers becomes possible with tractography techniques. There are many approaches that can be used do to this, each with its own advantages and limitations, as described in subsection 1.2.6.
In this section, the physical process of molecular diffusion and the imaging technique that allows to study the diffusion phenomenon will be firstly presented. Then the indices that quantify the type of diffusional process will be discussed. The chapter ends with a comparison between the two tractography techniques that can be used to create a 3D representation of the fibers.

### 1.2.1 Molecular diffusion

DTI is an MR technique sensitive to diffusive properties of water molecules. Molecular diffusion is the result of the translational movement of molecules via thermally driven random motions, the so called Brownian motion. The mathematical expression that describes the mobility of the molecules, was formulated by Albert Einstein in 1905 and is expressed by the following equation:

$$< r^2 >= 2 \cdot D \cdot T_d \tag{1.1}$$

where $< r^2 >$ is the mean diffusion distance (mm), $T_d$ is the diffusion time (s) and $D$ is the diffusion coefficient (mm$^2$/s). This last coefficient is defined by the Stokes-Einstein equation (1.2) and describes the diffusion coefficient of a spherical particle in a viscous fluid:

$$D = \frac{k_B \cdot T_d}{6\pi \cdot r_p \cdot \eta} \tag{1.2}$$

where $k_B$ is the Boltzmann's constant (J/K), $r_p$ is the particle's radius, $\eta$ is the viscosity of the fluid.
The diffusion coefficient for free water at $37°C$ is equal to $3 \cdot 10^{-9} m^2 s^{-1}$, however in the tissues it decreases for the presence of physiological barriers, such as cellular membranes, macromolecules and fibers, which decrease the mobility of the molecules. Therefore, the diffusion coefficient is an hallmark of the integrity and the functionality of tissues and can be used to identify possible pathological alterations.

### Isotropic diffusion

Water molecules in the brain are constantly moving (in Brownian motion). When motion is unconstrained, as in the large fluid-filled spaces deep in the brain (e.g., the ventricles, as illustrated in Figure 1.4), diffusion is isotropic, which means that motion occurs equally and randomly in all directions. In this case the displacements of the water molecules can be described by a Gaussian distribution along one axis (e.g., x):

$$\frac{1}{\sigma\sqrt{2\pi}} e^{-x^2/2\sigma^2} \tag{1.3}$$

where $1/\sigma\sqrt{2\pi}$ is the scaling factor to normalize the area under the curve to 1. In our case, the parameters $\sigma$, which controls the width of the curve, tells us how far water molecules travel on average, so it is equal to the mean diffusion distance r. Therefore, by using equation (1.1), $\sigma$ is equal to $\sqrt{2DT_d}$; by substituting this equation in equation (1.3) we can obtain the population of water molecules that moved along x at a generic time point t:

$$P(x,t) = \frac{1}{\sqrt{4\pi Dt}} e^{-x^2/4Dt} \tag{1.4}$$

This shows that the longer is the time passed (t), the wider the distribution becomes. For fixed t, higher diffusion constants lead to a wider distribution [9]. Moving in a three-dimensional space, the Gaussian distribution becomes:

$$P(r,t) = \frac{1}{\sqrt{(4\pi Dt)^3}} e^{-r^T r/4Dt} = \frac{1}{\sqrt{(4\pi Dt)^3}} e^{-\frac{x^2+y^2+z^2}{4Dt}} \tag{1.5}$$

This surface is called "Diffusion sphere" when the sphere radius is equal to the square root of the quantity defined by equation (1.1) :

$$x^2 + y^2 + z^2 = (\sqrt{2Dt})^2 \tag{1.6}$$

Therefore, the particle motion is characterized by a single value of D, equal along the three directions, and thus it is impossible to identify a preferential direction, as shown in Figure 1.4.

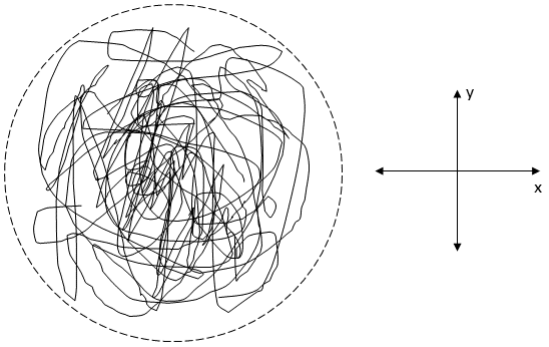


Figure 1.4: Isotropic diffusion in a 2D space. Water molecules do not move along a preferential direction; the motion is random.

### Anisotropic diffusion

We talk about anisotropic diffusion when the motion of the molecules is constrained to follow a preferential direction, as in white-matter tracts (see Figure 1.5). To characterize this type of motion the constant diffusion coefficient D is not enough anymore, therefore we can introduce the diffusion tensor $\mathbf{D}$:

$$\begin{bmatrix} D_{xx} & D_{xy} & D_{xz} \\ D_{yx} & D_{yy} & D_{yz} \\ D_{zx} & D_{zy} & D_{zz} \end{bmatrix}$$

This is a symmetric tensor, i.e. $D_{ij} = D_{ji}$ for $i \neq j$ and this means that for its complete description, six coefficients, instead of nine, are sufficient. In an anisotropic medium, the Gaussian distribution becomes:

$$P(r,t) = \frac{1}{\sqrt{(4\pi|\mathbf{D}|t)^3}} e^{-r^T \cdot \mathbf{D} \cdot r/4t} \tag{1.7}$$

and the surface described by equation 1.7 is called "diffusion ellipsoid" and it has one principal axis, which corresponds to the direction in which the major diffusion coefficient is registered.

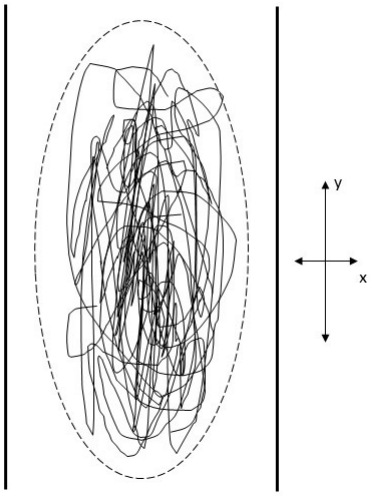


Figure 1.5: Anisotropic diffusion in a 2D space: the motion is oriented more in one direction (along y axis) than in the others.

### 1.2.2 Diffusion MR signal

The effect of diffusion on the MR signal was first noted by Hahn in 1959 [11] and later by Carr and Purcell in 1954 [12]. In 1956 Torrey, by adapting the Bloch equations, created the so-called Bloch-Torrey Equation [13]. In 1965 Stejskal and Tanner performed an experiment called "Pulsed gradient spin echo (PGSE)", which allowed to do the first quantitative measurements of molecular diffusion [14]. The protons are the responsible of the signal measured with MR. With no external magnetic field, spins have random spatial orientations and thus zero net sum. The application of a high external and stationary magnetic field ($B_0$) at high intensity (0.3-3T in clinical practice) causes the protons' spins to align with it. After ($B_0$) application, a perturbation is applied for few milliseconds and after it the system returns to the non-perturbed state. This perturbation is caused by the magnetic field ($B_1$) perpendicular to ($B_0$) and at low intensity ($\mu$T). After the removal of the ($B_1$) field, the magnetization of the protons returns to its initial conditions through relaxation phenomena and the Free Induction Decay (FID) signal, which reflects the loss of residual magnetization, is measured.
The Stejskal-Tanner sequence is a particular spin-echo sequence that allows to obtain an MR signal bound to the diffusion coefficient. The sequence consists of one 90° radio-frequency pulse followed by a second one of 180°. The first pulse allows the spins, previously aligned to the $B_0$ field, to orient themselves to the plane perpendicular to the direction of the magnetization vector. Spins in this condition start oscillating at the Larmor frequency and the magnetization vector returns to the condition preceding the application of the 90° pulse through loss of spin-spin magnetization according to a time T2, called "transversal relaxation". The application of the second 180° pulse allows the inversion of the spins. After

a certain time, called "echo time (TE)" and about 10-100ms, the residual magnetization MR signal is measured.
To cause the inhomogeneities that allow to generate an MR signal sensitive to the diffusive motion of water molecules, short-term gradients have to be applied before and after the 180° pulse, as shown in Figure 1.6. The application of a magnetic field gradient pulse along one axis, e.g. x axis, creates a dephasing $\phi_i$ of the magnetic moment $\mu$ associated to the spin, that is function of the position $x_i$ of the spin along the x axis. The dephasing is defined as:

$$\phi_i = \int_0^{\delta} \gamma G x_i dt \tag{1.8}$$

where G is the intensity of the gradient applied along the x direction, $\delta$ is its duration and $\gamma$ the gyromagnetic ratio (2.7653108 rad/s·T).
If the spin is stationary, the application of two successive and opposite gradient pulses (i.e. with the same direction, but opposite amplitude for rephasing the spins), causes the phase shift to be null. Whereas, if the spin is exposed to a diffusion process during the time interval $\Delta t$ that elapses between the two gradient pulses and moves from position $x_1$ to $x_2$, it undergoes a net phase shift $\Delta\phi$ equals to:

$$\Delta\phi = \phi_1 - \phi_2 = \gamma\delta G x_1 - \gamma\delta G x_2 = \gamma\delta G\Delta x \tag{1.9}$$

Therefore nuclear spins will encounter a dephasing that will translate in a total magnetization reduction, as described in Figure 1.7.

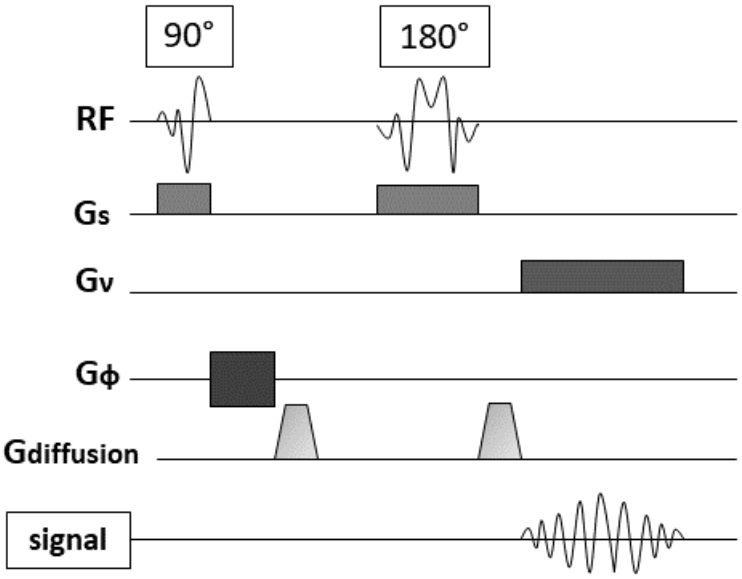


Figure 1.6: Schematic representation of the Stejskal-Tanner sequence: a traditional spin-echo sequence with the addition of a diffusion gradient. Adapted from [15].

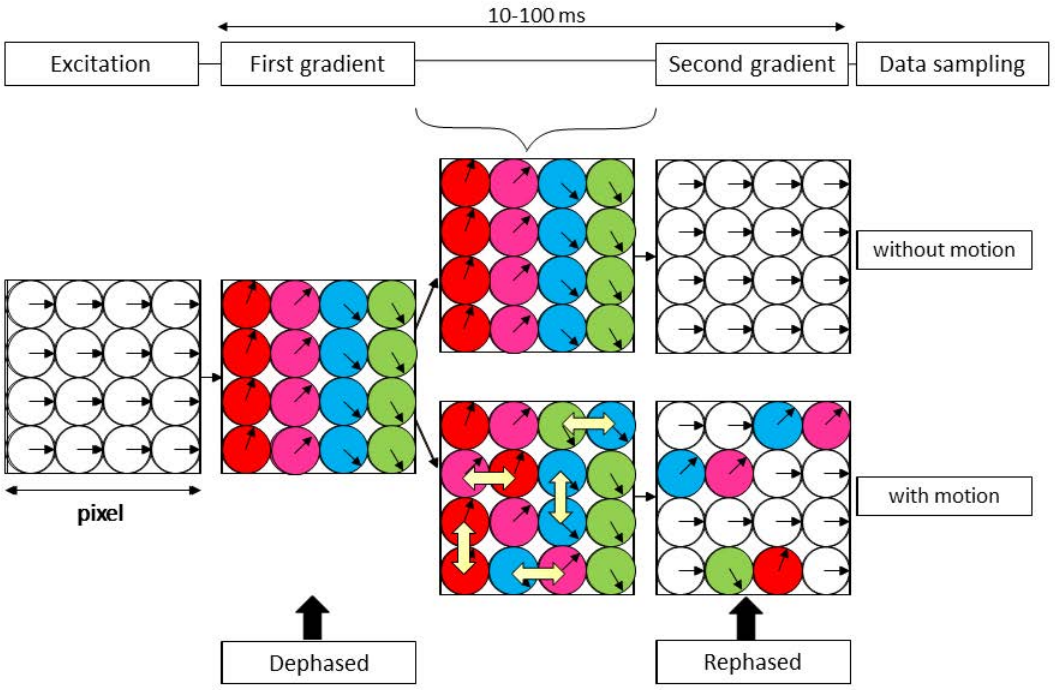


Figure 1.7: Illustration showing the relationship between water motion and gradient application. Each circle represents water molecules at different locations within a voxel. The vectors in the circles indicate phases of the signal at each location. If water molecules move between the two gradient applications, the second pulse cannot perfectly refocus the phases, which leads to signal loss. Adapted from [16].

### 1.2.3 Diffusion Weighted Imaging (DWI)

To completely characterize an isotropic diffusion process, it is sufficient to determine the value of the diffusion coefficient D, which is constant in this case.
With the Stejskal-Tanner sequence, the MR signal depends on $S_0$, the signal registered without the application of the gradient G, on the diffusion coefficient D and on the so-called "b-value", according to the relation:

$$S = S_0 e^{-b \cdot D} \tag{1.10}$$

The b-value parameter, measured in $s/mm^2$ depends on the experimental design and it is defined as:

$$b = (\gamma \delta G)^2 t_d = (\gamma \delta G)^2 (\Delta t - \frac{\delta}{3}) \tag{1.11}$$

where G is the value of the gradient (mT/m), $\delta$ its duration (ms) and $\Delta t$ the time elapsed between the application of two successive gradients (ms). To neglect diffusion phenomena that may occur during the gradient application, the condition

$\delta \ll \Delta t$ must be verified. Under this assumption the b-value assumes this form:

$$b = (\gamma \delta G)^2)\Delta t \tag{1.12}$$

By substituting this in equation (1.10) and assuming that the b-value is completely known, one can obtain the following equation in the unknowns $S_0$ and D:

$$ln(\frac{S}{S_0}) = -b \cdot D \tag{1.13}$$

Therefore, at least two measurements are required to solve this equation. Equation (1.13) also shows that the value of the diffusion coefficient D can be recovered by measuring the trend of the intensity logarithm of the signal as a function of b, known parameter that changes depending on the sequence adopted, as shown in Figure 1.8. When a single b-value is used, the DTI acquisition is called "mono-shell", while when more than a b-value is adopted the acquisition is called "multi-shell".
One can also note that:

- higher b-values lead to a higher weight of the diffusion effect
- by decreasing the b-value, the signal-to-noise-ratio (SNR) increases (see Figure 1.9)
- an increase in the b-value leads to an increase in the acquisition time

Diffusion has been described until now as a microscopic phenomenon: in the same voxel many microstructures and compartments with different diffusion coefficients can be found. Under the assumption that diffusion time is sufficiently small to discard diffusion phenomena between voxels, the attenuation of the signal can be described by a multi-compartmental model through the following formula:

$$\frac{S}{S_0} = \sum_i p_i e^{-bD_i} \tag{1.14}$$

where $D_i$ and $p_i$ are respectively the diffusion coefficient and the molecular fraction that diffuse in the i-th voxel.
The ideal approach would be to estimate all the $D_i$ coefficients with a multi-exponential fit, but this is not possible because of their intensity and variability, which are often limited. It is therefore preferred to estimate the value of the Apparent Diffusion Coefficient (ADC) defined as:

$$ADC = \sum_i p_i D_i \tag{1.15}$$

By modeling the signal with ADC and by substituting in equation (1.13) one can obtain:

$$ln(\frac{S}{S_0}) = -ADC \cdot b \tag{1.16}$$

ADC coefficient is determined in the same way as the diffusion coefficient D. By estimating the ADC value for each voxel, maps related to the diffusion process, but not to its directionality, can be obtained. In these maps the ADC value is lower if the signal intensity is higher and viceversa, as shown in Figure 1.10.

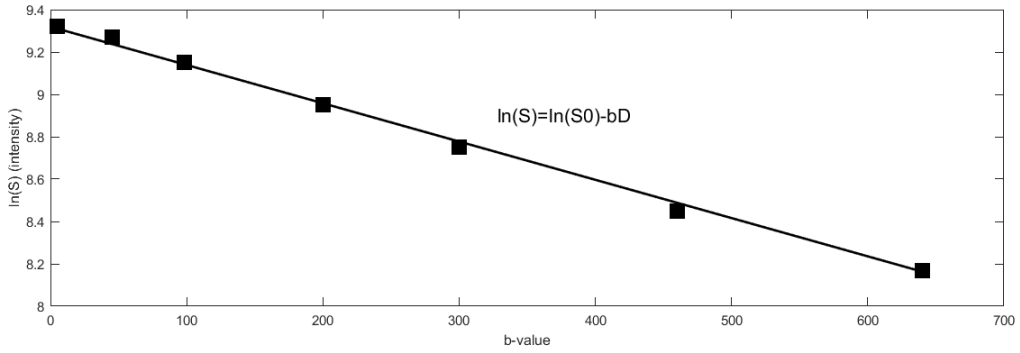


Figure 1.8: Plot of results obtained using equation (1.13) and seven different b-values. The diffusion coefficient D is given by the slope of the line. Adapted from [16].

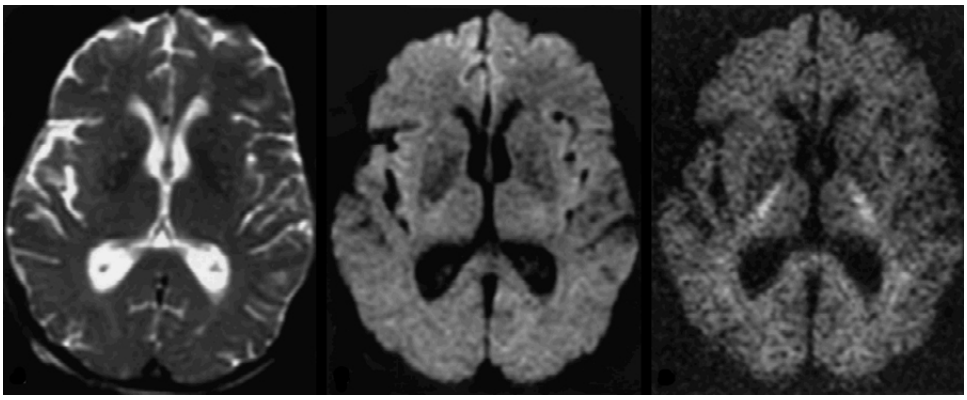

Figure 1.9: Brain diffusion-weighted images using 3 different b-values (axial view): 0, 1000 and 3000 s/mm$^2$. Taken from [17].

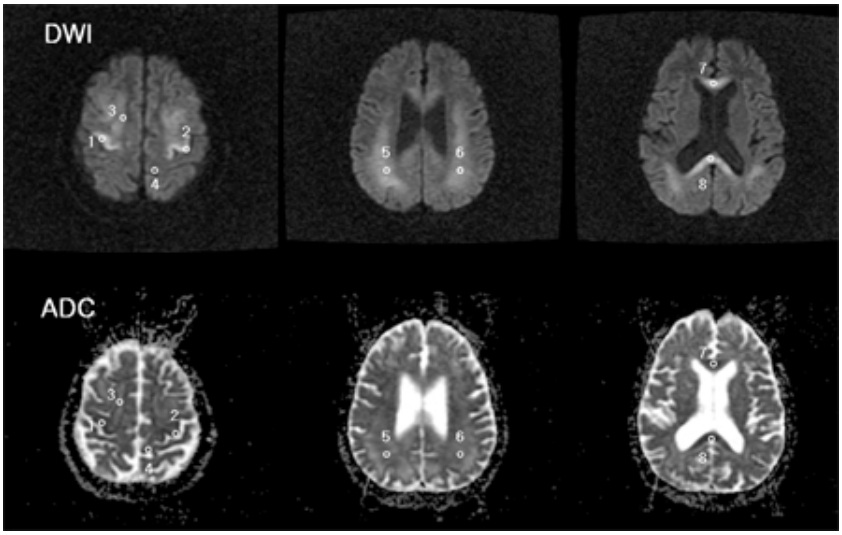


Figure 1.10: Comparison between signal intensities on diffusion-weighted images (upper row) and ADC values (bottom row). Hyperintensity areas are those in which the diffusion signal is higher, while hypointensity areas correspond to a lower diffusion signal. ADC values are markedly reduced in regions with high signal intensity on diffusion-weighted images. Taken from [18].

### 1.2.4 Extraction of the diffusion tensor

In those tissues where the molecular motion is anisotropic, the diffusion coefficient is not constant anymore, but it assumes the form of a tensor. Therefore, the equation (1.10) is modified as follows:

$$S = S_0 e^{-\sqrt{\mathbf{b}}\cdot\mathbf{D}\cdot\sqrt{\mathbf{b}^T}} \tag{1.17}$$

where $\mathbf{b}$ is now a vector and it is called "b-vector". Exploiting the symmetry properties of the diffusion tensor $\mathbf{D}$, equation (1.17) becomes:

$$ln(\frac{S}{S_0}) = -\left[\begin{array}{ccc}\sqrt{b_x} & \sqrt{b_y} & \sqrt{b_z}\end{array}\right]\left[\begin{array}{ccc}D_{xx} & D_{xy} & D_{xz}\\ D_{yx} & D_{yy} & D_{yz}\\ D_{zx} & D_{zy} & D_{zz}\end{array}\right]\left[\begin{array}{c}\sqrt{b_x}\\ \sqrt{b_y}\\ \sqrt{b_z}\end{array}\right] \tag{1.18}$$

$$ln\frac{S}{S_0} = -(D_{xx}b_x + D_{yy}b_y + D_{zz}b_z + 2D_{xy}\sqrt{b_xb_y} + 2D_{xz}\sqrt{b_xb_z} + 2D_{yz}\sqrt{b_yb_z}) \tag{1.19}$$

Now, defining the following vectors:

$$\overline{\mathbf{b}} = [b_x b_y b_z \sqrt{b_xb_y}\sqrt{b_xb_z}\sqrt{b_yb_z}] \text{ and } \overline{\mathbf{D}} = [D_{xx}D_{yy}D_{zz}2D_{xy}2D_{xz}2D_{yz}]^T$$

equation (1.19) can be rewritten in a compact form:

$$ln(\frac{S}{S_0}) = \mathbf{A} = -\overline{\mathbf{D}}\cdot\overline{\mathbf{b}} \tag{1.20}$$

Hence, to determine completely the diffusion tensor, it is necessary to measure at least six images ($S_i$ with i=1,...6) along six non-collinear directions (chosen to uniformly sample the 3D-space) in addition to a diffusion non-weighted image ($S_0$).
The resulted systems is:

$$\begin{bmatrix} ln(S_1/S_0) \\ ln(S_2/S_0) \\ ln(S_3/S_0) \\ ln(S_4/S_0) \\ ln(S_5/S_0) \\ ln(S_6/S_0) \end{bmatrix} = - \begin{bmatrix} \overline{b_1} \\ \overline{b_2} \\ \overline{b_3} \\ \overline{b_4} \\ \overline{b_5} \\ \overline{b_6} \end{bmatrix} \cdot \overline{\mathbf{D}} \tag{1.21}$$

and it can be solved through the linear least squares (LLS) method:

$$\mathbf{D} = -(\overline{\mathbf{b}}^T \overline{\mathbf{b}})^{-1} \overline{\mathbf{b}}^T \mathbf{A} \tag{1.22}$$

or through the weighted linear least squares (WLLS) method, if additional information regarding the measurement error are available. In this case the solution of system (1.21) is:

$$\mathbf{D} = -(\overline{\mathbf{b}}^T \Sigma^{-1} \overline{\mathbf{b}})^{-1} \overline{\mathbf{b}}^T \Sigma^{-1} \mathbf{A} \tag{1.23}$$

where $\Sigma$ is the covariance matrix of the estimate error, which contains the reciprocal of the square of the transformed log data.
This problem can be solved also with nonlinear approaches, which aim to determine the parameters directly from the fit of the non transformed log data.
Although six directions are sufficient for the estimation of $\mathbf{D}$, a better estimate of the tensor elements can be achieved acquiring more than six images; commonly 32, 64 or 128 directions are used.
After estimating the constitutive parameters, it is possible to reconstruct the tensor $\mathbf{D}$ and thus obtain, through the diagonalization operation, the eigenvalues ($\lambda_1$,$\lambda_2$,$\lambda_3$) and associated eigenvectors ($v_1$,$v_2$,$v_3$). The eigenvectors are representative of the principal directions of diffusion, while the eigenvalues quantify the intensity of the diffusive process along these directions.

### 1.2.5 Diffusion indices

Once obtained the six parameters of the diffusion ellipsoid at each voxel, the next task is to visualize it to appreciate the neuroanatomy of the region under investigation [9]. The information contained in the eigenvalues and eigenvectors can be exploited to derive representative maps of the diffusion process.
By defining $v_1$ as the major eigenvector, which is assumed to represent the local fiber orientation, and $\lambda_1$ the corresponding eigenvalue and combing conveniently the remaining parameters ($v_2$,$v_3$,$\lambda_2$,$\lambda_3$), many diffusion indices can be defined. These metrics reduce the 6D information of the tensor to a simple 1D scalar,

which represents only a small part of the tensor information and can be visualized as a gray or color scale map. These images can be easily interpreted and used as a first step toward the identification of normal and pathological tissue [19].
The indices can be divided in two main groups: rotationally variant and rotationally invariant [20].
The main rotationally variant indices are:

- **Axial Diffusivity (AD)**: it is the value of the major eigenvalue $\lambda_1$ and it measures the diffusivity along the major diffusion direction

- **Radial Diffusivity (RD)**: given by the mean of the minor eigenvalues, it represents the diffusion process that takes place in the normal direction respect to $v_1$:

$$RD = \frac{\lambda_2 + \lambda_3}{2} \tag{1.24}$$

- **Mean Diffusivity (MD)**: defined as the mean of the eigenvalues, it represents the mean intensity of the diffusion tensor:

$$MD = \overline{\lambda} = \frac{\lambda_1 + \lambda_2 + \lambda_3}{3} \tag{1.25}$$

The rotationally invariant indices, which are not related to the reference system, provide an objective and intrinsic measure of the structure. The main indices are [9]:

- **Fractional Anisotropy (FA)**: it is the most common measure that quantifies anisotropy and determines the fraction of the diffusion tensor that can be ascribed to anisotropic diffusion. FA is calculated as the normalized variance of the three eigenvalues:

$$FA = \sqrt{\frac{1}{2}} \frac{\sqrt{(\lambda_1 - \lambda_2)^2 + (\lambda_2 - \lambda_3)^2 + (\lambda_3 - \lambda_1)^2}}{\sqrt{\lambda_1^2 + \lambda_2^2 + \lambda_3^2}} \tag{1.26}$$

  For an isotropic medium, FA=0, while for a cylindrically symmetric anisotropic medium (i.e. with $\lambda_1 \gg \lambda_2 = \lambda_3$), FA=1.

- **Relative Anisotropy (RA)**: it is a measure derived from the ratio of the anisotropic portion of the diffusion tensor to the isotropic portion:

$$RA = \sqrt{\frac{1}{2}} \frac{\sqrt{(\lambda_1 - \lambda_2)^2 + (\lambda_2 - \lambda_3)^2 + (\lambda_3 - \lambda_1)^2}}{\lambda_1 + \lambda_2 + \lambda_3} \tag{1.27}$$

  For a purely isotropic medium, RA=0, whereas for a highly anisotropic, cylindrically symmetric medium RA tends towards $\sqrt{2}$ [21].

- **Volume Ratio (VR)**: it is the ratio between the volume of the ellipsoid, represented by the diffusion tensor, and the volume of a diffusion sphere of radius equals to $\overline{\lambda}$:

$$VR = \frac{\lambda_1 \cdot \lambda_2 \cdot \lambda_3}{[(\lambda_1 + \lambda_2 + \lambda_3)/3]^3} = \frac{\lambda_1 \cdot \lambda_2 \cdot \lambda_3}{\overline{\lambda}^3} \tag{1.28}$$

  It assumes values in the [0,1] range, where VR=0 corresponds to the maximum value of anisotropy and VR=1 to the maximum of isotropy.

In Figure 1.11 some example maps, representing different indices, are displayed.

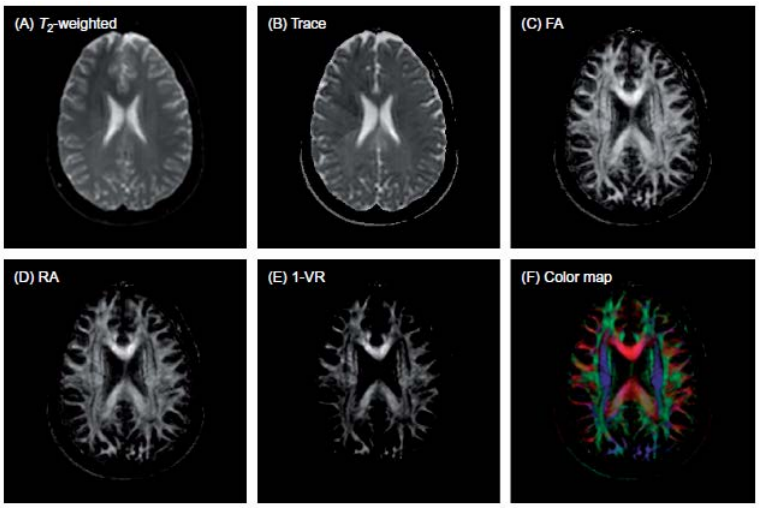


Figure 1.11: Example indices obtained from DTI. (A) Reference $T_2$-weighted image; (B) trace map obtained from the sum of the eigenvalues; (C) fractional anisotropy (FA) map; (D) relative anisotropy (RA) map; (E) volume ratio (VR) map; (F) color-coded orientation map. In the RGB map, red, green and blue represent fibers running along the right-left, anterior-posterior and superior-inferior axes, respectively. Taken from [9].

Although rich of information, these indices derived from eigenvalues lack one important information measured with DTI, that is the orientation of the fibers, which is contained in the eigenvectors.
The major eigenvector $v_1$ is assumed to represent the local fiber orientation, therefore in many studies $v_2$ and $v_3$ are discarded. The major eigenvector $v_1$ is a unit vector; defining its components [x,y,z] in the 0-1 range, it satisfies the criterion $x^2 + y^2 + z^2 = 1$.
These x, y and z components can be presented separately as grayscale maps. To obtain cleaner and more informative images, low-anisotropy regions can be masked by multiplying the vector-component images by an anisotropy map such as FA, thus obtaining FA-weighted vector-component images in gray-scale. To better visualize fiber orientations in one image, a 24-bit color presentation, which uses RGB channels, is employed: the x, y and z component images are assigned

to three RGB principal colors and combined to make one color-coded map [9] (see Figure 1.11f). Figure 1.12 displays the steps required to derive this color-coded orientation map.

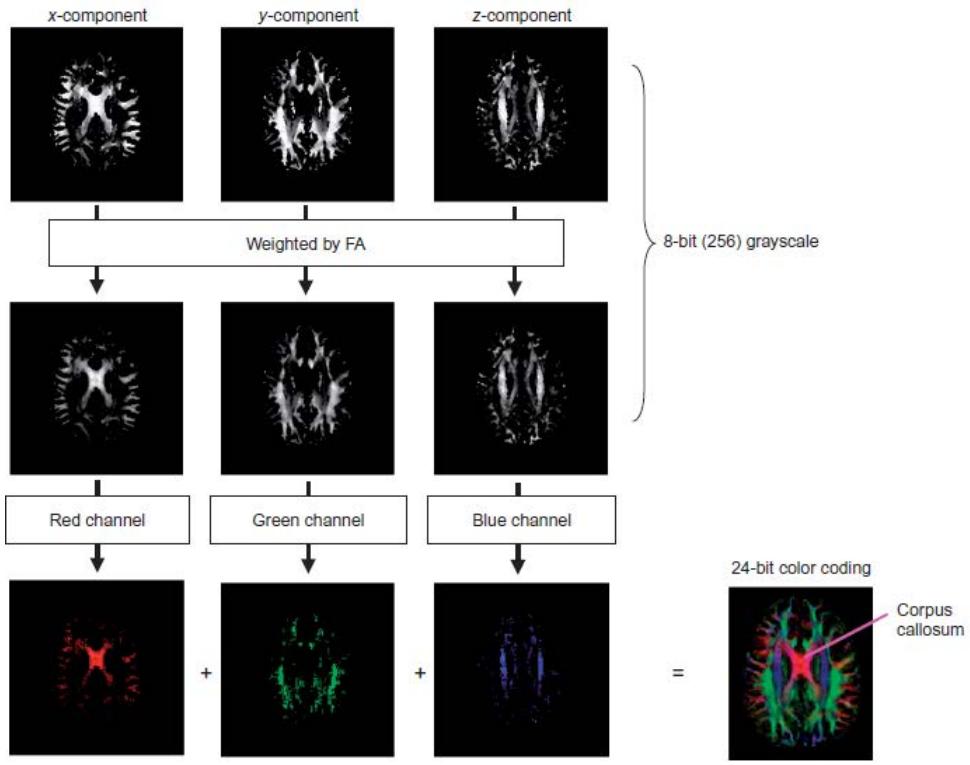


Figure 1.12: Steps needed to create a color-coded fiber orientation map. The x, y and z components are those of the major eigenvector $v_1$. Taken from [9].

### 1.2.6 Fiber tracking

DTI fiber tracking is a powerful tool for the study of white-matter connectivity between voxels in the brain. The aim of DTI fiber tracking is to both localize and assess the specific neuronal pathways and then to link this information with the anatomical one, measured with standard neuroradiological examinations [22] [23]. This combination between DTI fiber tracking, which is a low spatial resolution technique (approximately 2x2x2mm), and higher resolution anatomical information, allows to better define specific pathways among brain regions.
Hence, 3D DTI tractography has opened up a new frontier for depicting human neuroanatomy noninvasively [24].
DTI fiber tracking algorithms can be divided into deterministic and probabilistic methods, as described below.

### Deterministic tractography

Deterministic approaches are based on the fundamental assumption that fiber trajectories, also known as "streamlines", follow the major eigenvector of the diffusion tensor, from voxel to voxel in a 3D-space. When the fiber trajectory reaches the edge of the voxel, the direction of the trajectory is changed to match the major eigenvector of the next voxel [24].
The streamline, considered as a continuous line, can be described as a 3D curve, i.e., a vector $\mathbf{r}(s)$, parameterized by the arc length, s, of the trajectory. The Frenet equation describing the evolution of $\mathbf{r}(s)$ is:

$$\frac{d\mathbf{r}(s)}{ds} = \mathbf{t}(s) \tag{1.29}$$

where $\mathbf{t}(s)$ is the unit tangent vector to $\mathbf{r}(s)$ at s. These vectors are depicted in Figure 1.13. Since the direction of the tangent vector $\mathbf{t}(s)$ corresponds to that of the principal eigenvector, $\mathbf{v}_1$, equation (1.29) can be rewritten as:

$$\frac{d\mathbf{r}(s)}{ds} = \mathbf{v_1}(\mathbf{r}(s)) \tag{1.30}$$

This system of three implicit differential equations can be solved by numerical methods, using the initial condition:

$$\mathbf{r}(0) = \mathbf{r}_0 \tag{1.31}$$

which specifies a starting point on the fiber tract, also known as "initial seed". The most common numerical methods, employed to solve eqs. (1.29) and (1.30), are the Euler's and the Runge-Kutta methods.

- **Euler's Method**
  The diffusion tensor $\mathrm{D}(\mathbf{r}(\mathrm{s}_0))$ is evaluated starting from the seed point $\mathbf{r}(\mathrm{s}_0)$. Then the Taylor series expansion of $\mathbf{r}(\mathrm{s})$ about $\mathbf{r}(\mathrm{s}_0)$ is used to evaluate the position of a nearby point on $\mathbf{r}(\mathrm{s}_0)$, $\mathbf{r}(\mathrm{s}_1)$:

  $$\mathbf{r}(s_1) = \mathbf{r}(s_0) + \mathbf{r'}(s_0) \cdot (s_1 - s_0) + ... \tag{1.32}$$

  Since the slope of $\mathbf{r}(\mathrm{s}_0)$ at $\mathrm{s}_0$, $\mathbf{r'}(\mathrm{s}_0)$, can be assumed to be parallel to $\mathrm{v}_1(\mathbf{r}(\mathrm{s}_0))$, a small number $\alpha$ (with $0 < |\alpha| \ll 1$) can be found such that satisfies:

  $$\mathbf{r'}(s_0) \cdot (s_1 - s_0) \sim \alpha \cdot \mathbf{v}_1 \cdot \mathbf{r}(s_0) \tag{1.33}$$

  Once the integration step $\alpha$ is chosen, we can write:

  $$\mathbf{r}(s_1) \sim \mathbf{r}(s_0) + \alpha \cdot \mathbf{v}_1 \cdot \mathbf{r}(s_0) \tag{1.34}$$

  $\mathbf{r}(\mathrm{s}_1)$ can be estimated from the value of $\mathbf{r}(\mathrm{s}_0)$ and $\mathbf{v}_1 \cdot \mathbf{r}(\mathrm{s}_0)$. This procedure can be repeated starting at the new point, $\mathbf{r}(\mathrm{s}_1)$ and can be iterated to predict the location of discrete points along the fiber trajectory, $\mathbf{r}(\mathrm{s})$ [22].

- **Runge-Kutta Method**
  The 2nd-order or the adaptive 4th-order Runge-Kutta methods should be preferred to the Euler's method since their estimates of higher derivatives of $\mathbf{r}(s)$ are more reliable. Furthermore, with these methods it is possible to control the amount of error introduced in each integration step by using an adaptive step sizing.

Deterministic streamlines propagation stops for four reasons:

1. the tract reaches the boundary of the imaging volume
2. the tract reaches a region with low diffusion anisotropy (FA$<$0.18)
3. the radius of curvature of the tract is smaller than approximately two voxels
4. the eigenvector that is the most collinear is not the same as the eigenvector associated with the largest eigenvalue

One of the problems of deterministic methods is that, at each iteration, the eigenvalues of the diffusion tensor are sorted according to their magnitude, associating the largest eigenvalue with $\mathbf{v}_1$. However, noise, patient movement and distortion from imaging artifacts, can cause these eigenvalues to be misclassified, consequently leading to a misclassification of their corresponding eigenvectors. While in areas of high SNR it is less likely to missort the eigenvalues, it occurs more frequently in less coherently organized white matter regions where the SNR is low. If this happens, $\mathbf{v}_1$ no longer represents the true direction of the fiber, thus causing the trajectory to suddenly go to the wrong direction [22].
Another important limit of this method is that it characterizes all the structures in a voxel with a single three variate (i.e. the 3 space directions) Gaussian distribution. Thus, if the voxel contains different kinds of structures or groups of structures of the same kind but with different microstructural or orientational characteristics, the diffusion tensor is a representation of the "average" diffusion properties in the voxel and fails to represent the actual microstructure. A classic example is the so-called "crossing fibers" problem: when two or more white matter bundles cross in a voxel, the estimated diffusion tensor is much more isotropic than it would be if only one of the bundles was present, and its first eigenvector is in a direction between those of the two bundles. In this case, the information derived by deterministic tractography does not represent the actual microstructural characteristics of the tissue. The same issue arises with more complex configurations in which more than one fiber direction is present, for example with fibers fanning or "kissing". Possible fibers' configurations are shown in Figure 1.14.

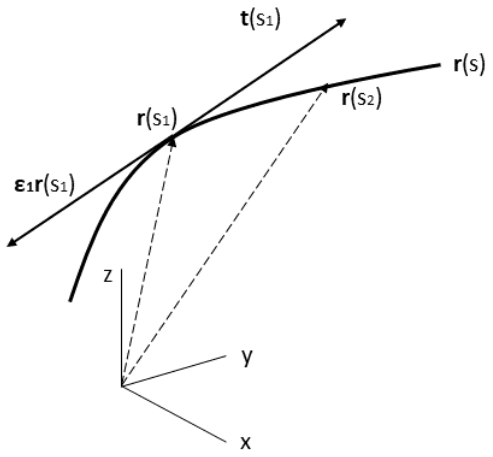


Figure 1.13: Representation of a streamline as a curve, $\mathbf{r}(s)$. The local tangent vector, $\mathbf{t}(s_1)$, is identified with the eigenvector, $\mathbf{v}_1(\mathbf{r}(s_1))$, associated with the largest eigenvalue of the diffusion tensor at position $\mathbf{r}(s_1)$. Adapted from [22].

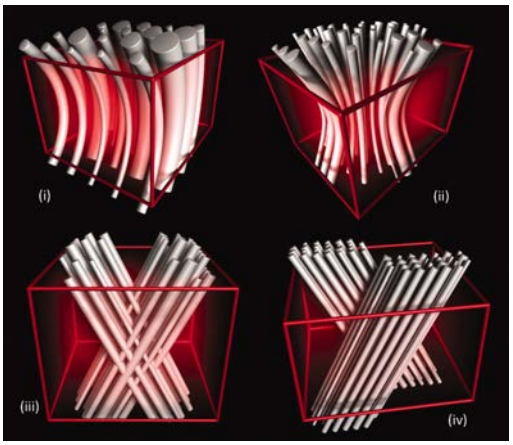


Figure 1.14: Simulated configurations of complex fiber bundle architecture at the length scale of a single voxel. Any tract organization is typically referred to as "crossing fibers" including (i) bending and (ii) fanning fiber bundles. The configuration shown in (iii) refers to interdigitating fibers, while that shown in (iv) reflects adjacent fiber bundles. Taken from [25].

### Probabilistic tractography

Probabilistic algorithms are computationally more expensive than deterministic ones, but can better deal with partial volume averaging effects and noise in the estimated fibre directions. Most importantly, the outputs of probabilistic algorithms are usually designed to give a connectivity index measuring how likely it is that two voxels are connected to one another.
Probabilistic fiber tracking methods can be divided in two main classes:

- **Advanced methods focused on microstructure**
  The objective of this class of methods is to better characterize biological tissues through a deep description of their microstructural features. For this purpose, these techniques precisely describe the statistical distribution of the displacements of water molecules in the different compartments of the tissue, and hence survey the presence and spatial organization of biological structures. Therefore, the main idea behind these methods is to go beyond the Gaussian model adopted for describing the diffusion process.
  Many models have been proposed in the last years, the more relevant are: DKI [26], Biexponential model [27], Ball and Stick [28], CHARMED [29], NODDI [30].

- **Advance methods focused on the estimation of fiber directions**
  The application of this class of methods requires the employment of the so-called High Angular Resolution Diffusion Imaging (HARDI), which consists in acquiring many diffusion-weighted images along multiple directions with a single b-value. These methods estimate the Orientation Distribution Function (ODF) that is the distribution of the fibers' directions in a voxel (see Figure 1.15). The main application of these approaches is the reconstruction of the trajectory of white matter bundles and the analysis of structural connectivity between brain areas, trying to resolve the crossing-fibers issue. The estimation of the ODF can be done through two different methods:

  - model independent methods: they estimate the diffusion-ODF profiles, which are directly related to the displacement of water molecules. DSI [31], QBI [32] [33], DOT [34], etc., belong to this class of methods.
  - model dependent methods: they estimate the fiber-ODF, which results sharper because it directly recovers underlying fiber orientations. Spherical deconvolution methods belong to this class and they are presented in detail, since they have been applied in this thesis.

### Spherical deconvolution

This method describes the HARDI signal in each voxel as the convolution between the fiber-ODF on a sphere and a kernel function that represents the "single fiber response", i.e. the signal one would observe if the fibers were perfectly aligned in each voxel. The ODF can thus be estimated as the spherical deconvolution of

the signal with this kernel [35]:

$$S(\mathbf{v}) = ODF(\mathbf{v}) \otimes h(\mathbf{v}) \tag{1.35}$$

where $\mathbf{v}$ is the unit vector of the diffusion gradient, h($\mathbf{v}$) is the system impulse response function or kernel and ODF($\mathbf{v}$) is the weight of the fiber response along each direction. The ODF can be simply estimated by matrix inversion, thus performing the spherical deconvolution operation. However, the spherical deconvolution problem is ill-posed and hence susceptible to noise. To solve this question, a low-pass filter can be used to attenuate or eliminate the high angular frequency components in the ODF. However, this leads to a decrease in the angular resolution [36], but without low-pass filtering, the noise would introduce large spurious negative lobes in the reconstructed ODF, which are physically not justifiable. An alternative way to reduce the ill-conditioning of spherical deconvolution operation consists in adding a constraint on the presence of these negative values in the ODF. Indeed, most white matter voxels contain contributions from few fibre bundles, thus the ODF will be null over most of its support, except for few peaks that correspond to the fiber orientations. Therefore, to reduce the high frequency noise that generates negative values, it is sufficient to eliminate any negative value in these regions of the ODF. For all these reasons the method described above is called Constrained Spherical Deconvolution (CSD). This method has been used in this thesis, since several studies [37] [38] demonstrated its superiority in the context of neurosurgical planning, when compared with DTI-based tractography. In Figure 1.16 results from a deterministic tractography method and CSD are compared.

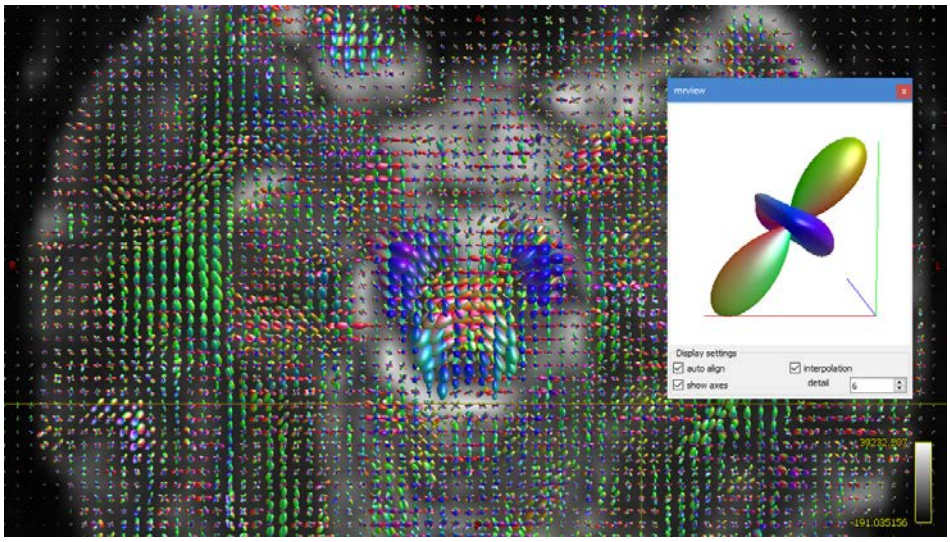


Figure 1.15: ODFs reconstructed for each voxel overlaid on the diffusion image. The box shows the ODF for an anisotropic voxel in which fibers follow more the antero-posterior direction indicated by the green ellipsoid.

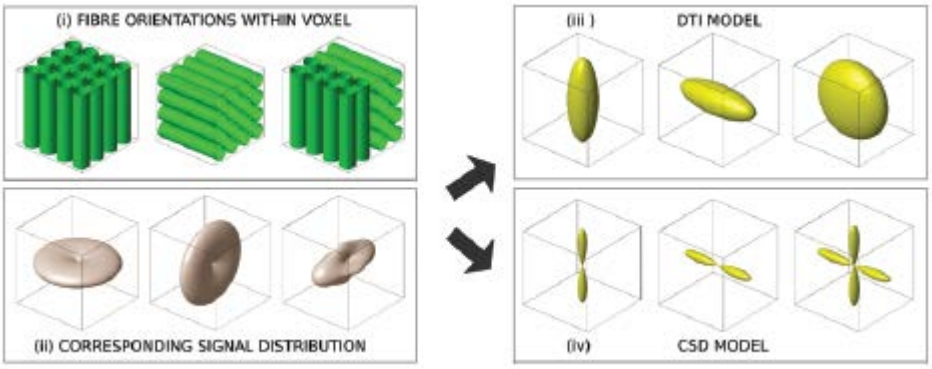


Figure 1.16: Comparison between DTI-based tractography and CSD methods. (i) Schematic images of voxels containing WM fibers (single fiber populations, left and middle; 2 fiber populations, right), (ii) corresponding DWI signal, (iii) diffusion tensor ellipsoids derived from the DWI signal within each voxel and (iv) fiber orientations derived using CSD. Note that in the voxel containing 2 fiber populations, the DTI model not only fails to represent the number of fiber populations within each voxel, but also does not provide an orientation estimate that corresponds to either of the constituent fiber populations. The CSD method instead correctly identifies 2 appropriately oriented fiber populations in the third voxel (see i). Taken from [41].

# Chapter 2

# Materials and methods

## 2.1 State of the art

Before starting this work, a bibliographic research was carried out to evaluate the state of the art in the use of DTI fiber tracking to predict the position and the course of FN in patients with vestibular schwannoma. The focus was mainly on two recent works by Song et al. [39] and by Yoshino et al. [40].
Song and colleagues [39] evaluated the use of fiber tracking for the preoperative determination of the facial nerve course in 15 patients with vestibular schwannomas. The MR data was collected using 3T MRI and the acquisition protocol includes T1-weighted and T2-weighted imaging, standard preoperative sequences, with the addition of a T1-weighted 3D FIESTA and the DTI scans. They employed a mono-shell DTI with a b-value of 1000s/mm$^2$ and 30 directions. 3D FIESTA was used to select the coordinates of the seeds through which the FN passed to help fiber tracking. The initial seed was set in the internal auditory canal, the passage seed was located within the connection between the internal auditory canal and the FN root exit zone (REZ) and the terminal seed in the REZ. The algorithm used for tracking was not specified, but they provided the parameters setting, reported in table 2.1. The validation of the results was performed by comparing the FN tracking with intraoperative FN electrophysiological monitoring. DTI fiber tracking was able to identify the facial nerve in 93.3% of patients. However, in only 92.9% of the patients, the reconstructed nerve was consistent with the surgical findings.
Yoshino and colleagues evaluated the use of fiber tractography to identify the location of the facial and cochlear nerves in 11 patients with vestibular schwannoma and who underwent tumor resection. MRI was performed using a 3T scanner and mono-shell DTI data was acquired along 30 gradient directions with a b-value of 1000s/mm$^2$, with an additional B0 image. They used the B0 image to place seed points in the internal auditory canal, to force the tracking to include the facial and vestibulocochlear nerves. Also in this work the tracking algorithm used was not specified. The parameters set in the algorithm are reported in table 2.1. For validation, visualized tracts were compared with locations of the facial and

cochlear nerves as identified by intraoperative electrophysiological monitoring. Their results showed that reconstructed tracts corresponded to the course of the facial or cochlear nerves in 81.8% of the cases and specifically to the FN course in 27.3% of cases and to the cochlear nerve in 54.5% of the cases.

| Work | Step size | Max angle | Min length | FA cutoff |
|---|---|---|---|---|
| Song et al. | 0.2mm | NA | 5mm | 0.1 |
| Yoshino et al. | 160mm | 30° | NA | 0.01 to the tracts' disappearance |

Table 2.1: Parameters settings for tracking algorithms in the two analyzed works. *Step size* set the step size of the algorithm; *Max angle* is the maximum angle between successive steps; *Min length* set the minimum length of any track; *FA cutoff* set the FA threshold for terminating tracks. NA = not available.

## 2.2 Patients

Pre-surgical data of 5 patients with vestibular schwannomas (VS) of different dimensions were acquired at the University Hospital of Padova (AOP) from March 2018 to July 2018. These patients underwent the surgery the day after the MR acquisition. The surgery was videotaped, so that the position and course of the facial nerve obtained through tractography could be compared with the real position and course found in vivo during the surgery.
In table 2.2 patients' information is reported.

| | Sex | Age | Symptoms | VS location |
|---|---|---|---|---|
| Patient 1 | F | 52 | deafness, right tinnitus, dizziness | right |
| Patient 2 | F | 57 | right earache, hearing loss | right |
| Patient 3 | F | 64 | tinnitus, right hearing loss | right |
| Patient 4 | M | 45 | tinnitus, right hearing loss | right |
| Patient 5 | M | 53 | tinnitus, left hearing loss | left |
| Mean±sd | | 54.2±6.9 | | |

Table 2.2: Dataset description

## 2.3 Acquisition protocol

The MRI data were acquired on a 3T Philips Inginia scanner at the Neuroradiology Department of the AOP.
The patients were administered the standard pre-surgical MR protocol with the supplement of a high-resolution T1-weighted and the multi-shell DTI acquisition. The sequences included in the acquisition protocol and the parameters set are

reported in table 2.3. In this standard protocol, high resolution anatomical images are acquired both before and after the injection of a contrast agent. The DTI acquisition was introduced before the administration of the contrast agent to the patient. Compared to previous studies, our DTI protocol was optimized to include multi-shell DTI acquisitions with several directions and two different phase encoding. The reasons why this new protocol should perform better than previous protocols are reported in the following:

1. The multi-shell DTI with several gradient's directions should allow to solve the crossing fibers issue and it is preferable in regions with low SNR like those of the cranial nerves. In particular, by using low b-values, vascular contributions can be eliminated whereas, by using high b-values, the fiber tracking algorithms are able to reconstruct more tracts. However, one must take into account that low b-values greatly reduce the angle of curvature that the tracking algorithms can solve, while high b-values can result in a high number of false positive.

2. The use of two DTI acquisitions with different phase encoding should help to correct the image distortions, as better explained in 2.4.

This optimized DTI protocol was developed keeping into consideration that the DTI acquisition had to be shorter than approximately 20 minutes to be tolerable for the patient. The total protocol proposed in this thesis is the maximum we could achieve with such time limitation. In table 2.4 the parameters of the two adopted DTI sequences are reported.

| Sequence | TR(ms) | TE(ms) | Voxel size (mm) |
|---|---|---|---|
| T1w | 7.8 | 3.6 | 0.5×0.5×1 |
| T2w coronal | 1900 | 80 | 0.5×0.5×0.5 |
| DTI | 5408 | 98 | 2×2×2 |
| Post-contrast HR T2w | 1500 | 241 | 0.2×0.2×0.2 |
| Post-contrast HR T1w | 5.8 | 3 | 0.4×0.4×0.5 |

Table 2.3: Parameters settings for the sequences included in the MR acquisition. TR= repetition time; TE= echo time; HR= high resolution. The same parameters were used in both DTI phase encoding sequences.

| Sequence | Phase encoding | FOV(mm) | b-values(s/mm$^2$) | N° directions |
|---|---|---|---|---|
| DTI-AP | antero-posterior | 2×2×2 | [0-0.1-300-1000-2000] | [1,11,8,32,64] |
| DTI-PA | postero-anterior | 2×2×2 | [0-0.1-300-1000] | [1,5,8,32] |

Table 2.4: Description of the two DTI sequences adopted in the MR protocol. FOV= field of view. Each number of directions refers to the corresponding b-value.

## 2.4 Data preprocessing

The MR data were recorded in DICOM format and then converted to NIFTI (Neuroimaging Informatics Technology Initiative) format [42] using the *dcm2niix* tool [43].
Like any other MRI technique, diffusion MRI is affected by artifacts, including image distortion, due to magnetic field inhomogeneity and to Eddy current effect, and motion artifacts. The distortion induced by magnetic field $B_0$ takes place when an object is placed in the MR scanner and thus disrupts the homogeneous field $B_0$, rendering the resulting field inhomogeneous.

**Distortion**
Since an object is made by different tissues that have different magnetic susceptibilities, the interface between these tissues and air causes dephasing of the spins, which creates signal loss and susceptibility and distortion artifacts [44]. The amount of distortion increases with the field strength: a 3T scanner produces more distortion than a 1.5T scanner [9].
Different techniques can be applied to correct geometric distortions that originate from $B_0$ inhomogeneities. Four of these field-map based methods are listed below:

- The first technique estimates the $B_0$ field inhomogeneity from phase images acquired at different echo times [45] [46].

- The second field map-based method uses the field maps derived from multi-echo gradient-echo images, which avoid complicated phase unwrapping procedures [47] [48].

- The third method utilizes image registration techniques for image distortion correction. The distorted image is coregistered to a corresponding anatomically correct MR image through an intensity-based least-squares similarity metric [49] or log-intensity metric [50]. This approach improves the sensitivity in areas of low diffusion signal.

- The last method is called "topup". It uses two or more acquisitions in which the mapping field distortions are different. A typical approach to apply topup is to use acquisitions with opposite phase-encoding polarities, in which the distortions go in opposite directions. From these images "topup" can estimate the field that maximises the similarity between unwarped volumes. The similarity is evaluated with the sum of squared differences between the unwarped images [51].

**Eddy currents**
Eddy currents are induced when strong gradient pulses are switched rapidly. Indeed, when the diffusion gradient pulses are switched on and off, the time-varying magnetic field of the gradients induces a current, called Eddy current, in the conductive surfaces of the MRI scanner and this current increases with the strength

of the gradient pulses. Eddy currents generate magnetic field gradients that vectorially combine with the gradient pulses such that the resulted gradients are not the same of those that were programmed to produce to final image. This error in the local gradients produces several types of geometric distortion in the final diffusion images: contraction or dilation of the image and overall shift and shear (Figure 2.1). These distortions are easy to recognize by comparing diffusion images with artifact-free anatomical images. The problem is that when gradient pulses become stronger, these distortions may become very large. A possible solution is to use a gradient coil of small dimensions placed as far as possible from the magnet core, which can generate larger gradient amplitudes. However, the best solution for Eddy currents is to adopt the so-called "self-shielded" gradient coils, which are a standard practice in the MRI system. These coils use additional wiring to decrease as much as possible the effects of the gradients outside the gradient coils. Nonetheless, Eddy currents may still arise in other parts (e.g. the RF coils), therefore the coils must be designed to reduce the amount of conductive parts. If residual Eddy currents remain, a possible method to be applied is the so-called "pre-emphasis", which consists in altering the shape of the currents sent to the gradient hardware. However, this operation is not easy because multiple corrections are needed [52].

**Motion**

Image misalignment artifacts are caused by subject movements during the DTI scans. If movements are wider that the size of the image voxels, the resulted DWIs will contain voxels not aligned for the entire duration of the scan. This issue can be easily corrected in a post-processing phase that consists in the realignment of the images through a 3D coregistration of multiple image volumes of the same subject. The 3D coregistration is usually achieved through rigid transformation that employs six parameters: three for rotation and three for translation. The realignment process involves the interpolation of the voxels, which leads to a smoothing effect and therefore in a loss of resolution and in a SNR enhancement [9].

**Denoising**

A further preprocessing step is the image denoising, which is necessary for the removal of thermal noise. The diffusion signal is sensitized to the stochastic thermal motion of water molecules and their interaction with surrounding microstructures, originated by diffusion gradients. Thermal noise, which corrupts DWI data, propagates to the parameters of interest and inhibits the quantitative interpretation of the results. Therefore, image denoising, which consists in minimizing the variance of the diffusion signal in a post-processing step, is an essential step to be performed. A possible approach to remove noise was proposed by Hotelling [53] and consists in decomposing a redundant dataset into a principal component basis and preserving only those components that are necessary for the description of the signal. This process is called "Principal Component Analysis (PCA)" and allows to obtain a dataset in which most of the signal vari-

ance is contained in few components (principal components), whereas the noise is spread over all components. A common criterion, also used in this thesis, to select the number of components that significantly contribute to the description of the diffusion process, includes the thresholding of the eigenvalues associated to the principal components [54].

**Optimized preprocessing pipeline**
In this work, imaging preprocessing was performed with different software, such as FSL [55], MRtrix [56], ANTs [57] and MATLAB [58].
The first step of the preprocessing was to integrate AP- and PA-DTI sequences, thus obtaining a diffusion image with a higher SNR and virtually distortion free compared to the single phase encoding. Diffusion image denoising and estimation of the noise level were performed using *MRtrix dwidenoise* function, while diffusion image pre-processing was done with *FSL eddy tool*, which includes inhomogeneity distortion correction using *FSL topup tool*. In Figure 2.2 are shown some diffusion acquired images, before and after the preprocessing step.
The second step of the preprocessing pipeline consisted in the registration of the DTI data with the T2-weighted image. Since the FOV of post-contrast high-resolution T2-weighted images was reduced compared to that of the DTI, a resampling of the T2-weighted data over the $B_0$ space was required. First, the $B_0$ image was extracted from the integrated diffusion images using *FSL fslroi* function, then a binary mask was created over the resampled image, to exclude those voxels of the image that were not of interest. The threshold for the mask was chosen manually based on the image intensity histogram. Secondly, using *ANTs Registration tool*, the resampled T2-w image was coregistered with the $B_0$ one, excluding the voxels inside the binary mask. The image registration adopted the rigid calibration mode, with 6 degrees of freedom, and used the MATTES metric [57].

## 2.5 Tractography analysis

Tractography analysis was performed with both the deterministic and probabilistic approaches, in both the tumor area and in its symmetric healthy counterpart in order to find the most suitable algorithm to track the FN course.

**Deterministic fiber tracking**
Deterministic fiber tracking was performed through the *FACT* (fiber assignment by continuous tracking) algorithm introduced by Mori et al. in 1999 [23]. Before the introduction of this method, tracking was performed by connecting each voxel to the adjacent one toward which the fiber direction was pointing. However, using this approach, the tracking often diverged from the true fiber orientation, because the choice of direction to follow was limited to only an 8 angle range, in the 2D space, or 26 in 3D space. This problem was avoided using the FACT algorithm, which tracks a continuous vector field instead of a discrete one (see

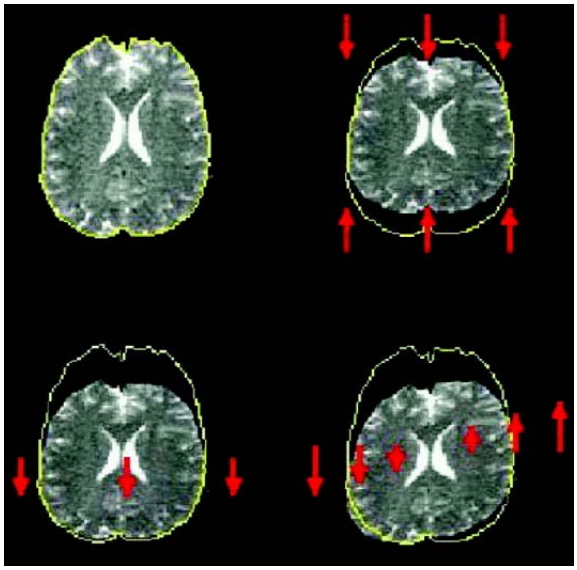

Figure 2.1: Examples of artifacts due to eddy currents: contraction (top right), shift (bottom left), and shear (bottom right). Taken from [52].

Figure 2.3). Tracking starts from the center of a voxel and proceeds according to the direction given by the eigenvector associated to the major eigenvalue. When the track leaves the voxel and enters the next, its direction changes according to that of the neighbor. Thanks to the presence of continuous intercepts, this tracking connects the correct voxels and the true path of the fiber can be assigned. The tracking is ended when vector orientation becomes random, therefore when the summation of the inner products of the eigenvectors is less than 0.8, according to the following equation:

$$R = \sum_{i}^{s} \sum_{j}^{s} abs(v_{\lambda_{1i}} \cdot v_{\lambda_{1j}})/s(s-1) \tag{2.1}$$

where $v_{\lambda_1}$ is the unit vector associated to the major eigenvalue $\lambda_1$ and s is the number of data points of reference. Although this method is able to overcome some problems, it has also some limitations:

- it can not discriminate among several small projections that are very close to each other
- it is not able to differentiate between afferent and efferent fibers
- it does not distinguish two paths that touch each other
- it can not track more than one branch of an axon

**Probabilistic fiber tracking**

Probabilistic fiber tracking was carried out using the Constrained Spherical Deconvolution (CSD) method, described in subsection 1.2.6. The response function

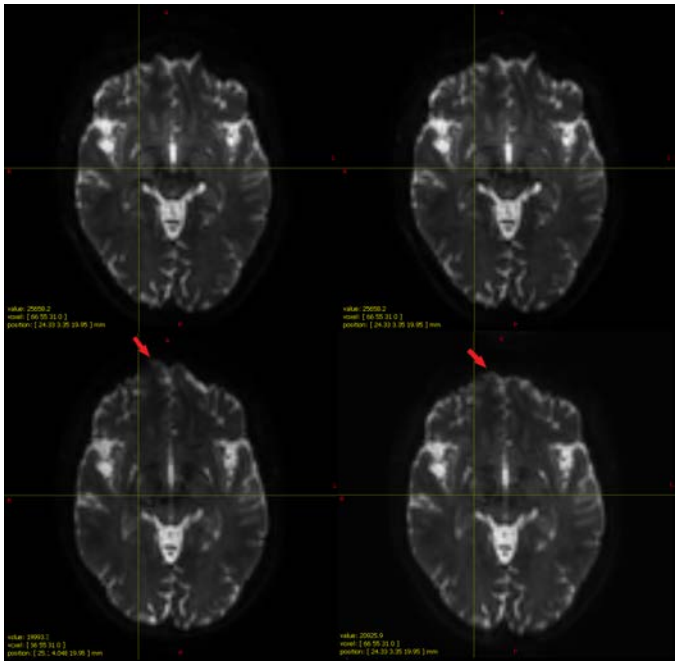

Figure 2.2: Axial view of the same slice for: DWI with AP-phase encoding (top left), DWI with PA-phase encoding (top right), integration between AP and PA sequences (bottom left), integrated DWI image after the preprocessing step (bottom right). The red arrow points to a region in which it is possible to see an image improvement thanks to these correction steps.

was estimated through *MRtrix dwi2response* function and the fiber orientation distributions through *MRtrix dwi2fod* function.
Two CSD-based methods were employed. The first CSD method used to track the FN was the *SD STREAM* algorithm. It takes as input an ODF image represented in the spherical harmonic (SH) basis, which contains the ODFs interpolated with a trilinear interpolation. At each streamline step, the local ODF is sampled and from the current streamline tangent orientation, a Newton-Raphson optimisation on the sphere is performed. This method allows to obtain an approximate solution for an equation of the type f(x)=0 and in this case it is used to locate the orientation of the nearest ODF amplitude peak [59].
The second CSD method used for the streamlines generation was the *iFOD2* method, based on $2^{nd}$ order integration over fiber orientation distributions. This algorithm steps along a path given by an arc of a circle of fixed length (the step-size), tangent to the current direction of tracking at the current point. The actual path selected for each step is obtained by sampling a probability density function (PDF) and the probability of each path is calculated as the product of the probabilities of each infinitesimal step making up that path. This probability is approximated by computing the product of the amplitude of the ODF, evaluated at regular intervals along the tangent to the path [37].
The SD STREAM method is less precise than the iFOD2 since it builds the fiber

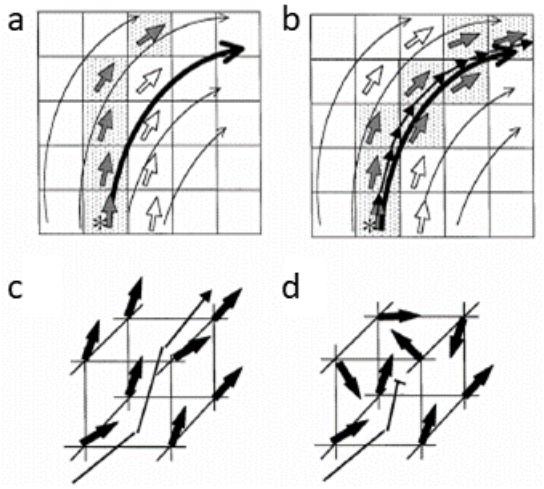


Figure 2.3: Tracking starts from the voxel with an asterisk and should follow the bold curved arrow. Curved arrows indicate the actual fibers, while open arrows indicate the average fiber direction in the voxel. The connected voxels resulting from tracking are shaded by dots. (a) The discrete approach does not reconstruct the correct pathway. (b) The continuous approach (FACT) tracks the correct pathway, as indicated by the train of solid arrows. (c) FACT algorithm is able to track 3D axonal projections as long as nearby vectors are strongly aligned. (d) When vector orientation becomes random, the algorithm stops. Adapted from [23].

path by applying the Newton-Raphson algorithm that builds an approximate solution of the nearest ODF peak. Furthermore, the iFOD2 algorithm should be able to track with higher accuracy than the SD STREAM in regions with crossing fibers, since iFOD2 employs a $2^{nd}$ order strategy and a step-size larger than that used in the SD STREAM method. The use of a step-size similar to voxel size should push to a more physiological reconstruction of the tracts. Therefore, if the interest is in having a high accuracy in the reconstruction of fiber paths, the best solution would be to use the iFOD2 algorithm. The SD STREAM method, which is computationally less demanding, could be successfully applied when fiber tracking is performed in high SNR regions containing fibers that do not cross each other.

**Common tractography steps**

The post-contrast T2-weighted image was used to infer prior anatomical information that could help the fiber tracking (e.g., position and size of the tumor, likely coordinates of the start, passage and end of the facial nerve). The coordinates of the seeds were selected, when possible, by an expert neuroradiologist to help the fiber tracking algorithm and they were set at the start, passage and end of the facial nerve. The radius of these seeds was set to 2mm, a reasonable value for including only the fibers that pass through that exact position. Additional masks, drawn manually in MRview [56], were created to remove all fibers reconstructed outside the area under investigation, separately for the healthy and unhealthy

regions. Then the tumor was segmented by using ITK-SNAP software [60] and it was provided as a region to be excluded during the streamlines generation in the tumor area. The streamlines generation, performed using the *MRtrix tckgen* and *tckedit* functions, was applied both in the tumor area and in its symmetric healthy counterpart, to display the course of the nerve in the area not affected by the tumor. The ROIs previously described were used also as either inclusion or exclusion criteria to constrain the fibers to pass through the provided seeds. Table 2.5 summarizes the parameters set for the *MRtrix tckgen* function, for the three tractography methods.

| Algorithm name | Type | N° streamlines | Step size |
|---|---|---|---|
| FACT | deterministic | 500000 | 0.2mm |
| SD STREAM | probabilistic | 500000 | 0.2mm |
| iFOD2 | probabilistic | 500000 | 1mm |

| Algorithm name | Max angle | Min length | FA cutoff | Seeds' radius |
|---|---|---|---|---|
| FACT | 9° | 10mm | 0.1 | 2mm |
| SD STREAM | 9° | 10mm | 0.1 | 2mm |
| iFOD2 | 45° | 10mm | 0.1 | 2mm |

Table 2.5: Parameters settings for tracking algorithms. *N° streamlines* is the number of streamlines to be selected; *Step size* sets the step size of the algorithm; *Max angle* is the maximum angle allowed between successive steps; *Min length* sets the minimum length of any track; *FA cutoff* sets the FA threshold for terminating tracks; *Seed radius* sets the radius of the sphere seed.

## 2.6 Total vs. reduced protocols

The next step consisted in applied the preprocessing pipeline and all three fiber tracking algorithms in both the total multi-shell DTI protocol and in the reduced DTI protocols. For each patient four reduced protocols were tested, extracting the data from the acquired available data:

- single-shell acquisition using only b=300s/mm$^2$
- single-shell acquisition using only b=1000s/mm$^2$
- single-shell acquisition using only b=2000s/mm$^2$
- multi-shell acquisition using all the directions for b=300s/mm$^2$, but randomly reducing to half of the original the directions for b=1000s/mm$^2$ and b=2000s/mm$^2$

The rationale for this analysis was to understand whether it was possible to reduce the total acquisition protocol and to obtain reliable results, thus speeding up the acquisition protocol and leading to a reduction in terms of costs and invasiveness for the patient.

## 2.7 Tumor classification

Before comparing the course of facial nerve obtained from DTI tractography with the in-vivo findings, the tumors of the 5 patients were classified according to different classification schemes. The tumor was classified according to its size, following the Sampath classification [62] and to its position, with respect to the pontocerebellar angle and the brainstem, according to Koos classification [63].
The Sampath classification divides the tumor in three groups based on its size:

- Group I: patients with tumors smaller than 2.5 cm in maximum dimension.
- Group II: patients with intermediate-sized tumors from 2.5 to 4 cm.
- Group III: patients with tumors larger than 4 cm in maximum dimension.

Koos grading system classifies tumors in four groups as follows:

1. Grade 1: small tumor developing in the auditory canal.
    - Type 1A: tumor indenting the vestibular nerve occipitally.
    - Type 1B: tumor indenting the vestibular nerve superiorly.
    - Type 1C: tumor indenting the vestibular nerve anteriorly.
2. Grade 2: small tumor with protrusion into the cerebellopontine angle (CPA), but not in contact with the brainstem from which the cranial nerves originate.
    - Type 2A: tumor interposed between nerve bundles of the vestibular and facial nerve.
    - Type 2B: tumor interposed between nerve bundles of the vestibular and facial nerve and separating the inferior and superior vestibular nerves.
3. Grade 3: tumor that occupies the cisternal part and does not dislocate the brainstem.
4. Grade 4: large tumor that displaces the brainstem and the cranial nerves.

Figure 2.4 displays the tumor grading system: higher degrees correspond to a greater extent of the tumor in the cisternal part.

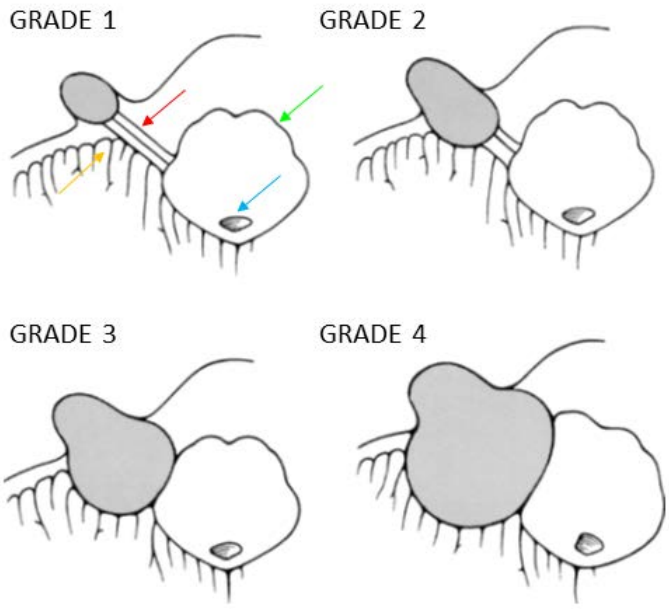


Figure 2.4: Illustrations of the adopted tumor grading system adopted. The red arrow indicates the cerebellopontine cistern, the orange arrow the cerebellopontine angle, the blue arrow the cranial nerves and the green arrow the brainstem. Adapted from [63].

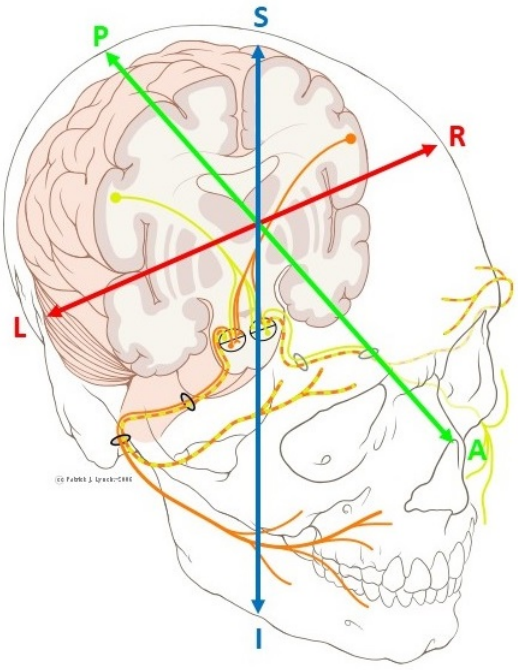


Figure 2.5: The course and the branches of facial nerve are represented by the yellow and orange lines. The colored arrows indicate the three directions that fibers can follow: green for antero-posterior, red for right-left, blue for superior-inferior. The convention adopted for the definition of the right-left direction is that used in radiology. Adapted from [61].

## 2.8 Qualitative analysis: Fiber tracking validation

To validate the fiber tracking results, several meetings were organized with neuro-radiologist, neurosurgeons, neurophysiologists and otolaryngologists who are part of this project. During these meetings, the position of the FN with respect to the tumor location found in-vivo was compared with that obtained with DTI tractography. A majority vote rule was applied to delineate the position of the nerve for each patient for both the in-vivo and the tractography results. The in-vivo analysis was carried out by the medical team looking at the videos recorded during the surgeries. The method described in [62], which divides the cochlear and facial nerve location into anterior, posterior or polar (around the upper or lower pole) was employed to classify the FN position relative to the tumor location. The anterior and posterior locations are further subdivided into superior, medial, or inferior thirds of the tumor capsule. The colored streamlines were instead visualized over the coregistered T2w image, focusing on those regions with a high

fiber density, calculated using the *MRtrix tckmap* function. Figure 2.5 shows the color legend of the streamlines: different colors mean different directions followed by the fibers.

## 2.9 Quantitative analysis

### 2.9.1 Total vs. reduced protocols

The comparison between the total and reduced protocols was carried out by assigning a score to the results of the tractography for the different methods and protocols. This score was assigned by three independent and expert observers who compared the reconstructed course of the FN nerve with its real in-vivo course, as shown in the recorded surgery tape. A score of 1 was assigned by each observer when there was agreement between in-vivo and reconstructed patterns, whereas a score of 0 was assigned otherwise. Individual observers' scores were then added together and a ranked in order to evaluate the best tractography method and the most appropriate protocol to use.

### 2.9.2 Metrics comparison

Maps of AD, ADC, FA and RD (see subsection 1.2.5) were obtained for each patient and for the only method (between FACT, SD STREAM and iFOD2) that in the previous analysis resulted successful. These maps were constructed starting from the preprocessed DWIs, by using the *MRtrix tensor2metric* function. The maps were then sampled to select only the values of the diffusion indices in the regions of reconstructed tracts, for the unhealthy FN locations. This analysis was performed to evaluate whether all or at least one of the diffusion indices could describe the microstructure of the fibers in these regions and whether there is any relationship between nerve integrity and functionality.

# Chapter 3

# Results

## 3.1 Tumor classification

Table 3.1 describes the dimensions, determined by the neurosurgeons, of the five analyzed schwannomas and their classification according to Koos and colleagues in [63] and explained in section 2.6. Table 3.2 displays a comparison between the percentage of frequency of VS size evaluated by Sampath and colleagues in [62] and that determined in this work. Tumors are classified in group I in all five patients and are of small size, according to the majority of the cases analyzed in [62].

| | VS size (mm) | VS grade |
|---|---|---|
| Patient 1 | 16×9 | 2A |
| Patient 2 | 13.5×6.5 | 2A |
| Patient 3 | 22×17 | 3 |
| Patient 4 | 15×13 | 3 |
| Patient 5 | 15.5×9.5 | 2A |

Table 3.1: Size of vestibular schwannoma, determined along the two perpendicular larger dimensions and its grade, according to Koos classification, in the five patients.

| | Group I | Group II | Group III | N° patients |
|---|---|---|---|---|
| Sampath et al. | 61% | 24% | 15% | 1006 |
| This work | 100% | 0% | 0% | 5 |

Table 3.2: Percentage of frequency of tumor size evaluated in [62] and in this work.

## 3.2 Qualitative analysis: Fiber tracking validation

Table 3.3 reports the location of facial nerve in relation to the VS position, evaluated at the origin of the FN in the brainstem and at the passage in the cerebellopontine cistern. In Figure 3.1, a further comparison with the findings of Sampath and colleagues [62], is displayed. In particular, the percentage frequencies of the sections in which the FN was found in the cisternal tract in relation to the VS, are compared with those found in [62].

| | Origin | Passage |
|---|---|---|
| Patient 1 | antero-inferior | antero-medial |
| Patient 2 | antero-inferior | antero-medial |
| Patient 3 | antero-medial | posterior (ribboned) |
| Patient 4 | antero-medial | antero-superior |
| Patient 5 | antero-medial | antero-superior |

Table 3.3: Location of FN compared to that of the VS, assessed at the origin of the nerve and in the cisternal passage tract.

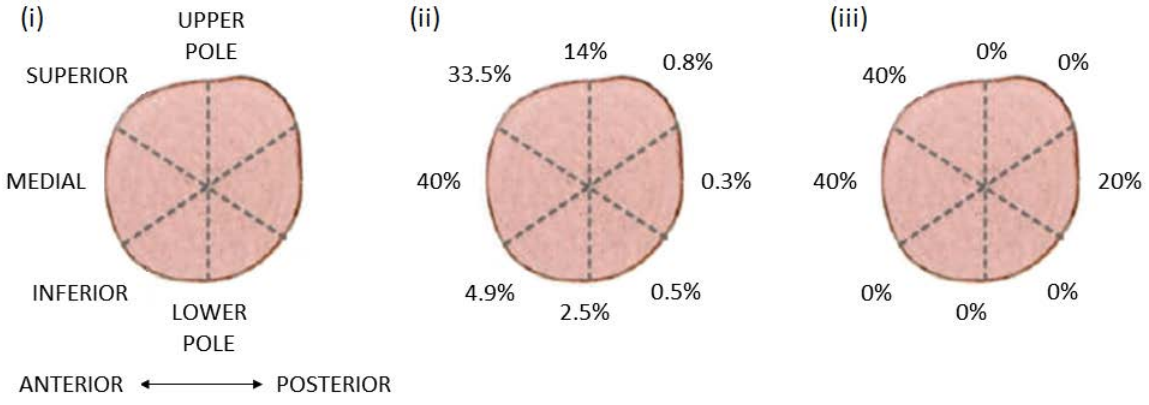


Figure 3.1: (i) Illustration showing a cross section of the VS with the possible locations in which the facial nerve could be found. (ii) Percentage frequencies of the sections in which the nerve was found in relation to tumor position, reported in [62]. (iii) Percentage frequencies of the sections in which the FN was found in patients acquired in this thesis work. Adapted from [62].

For each patient, a brief description of the FN course and its reconstruction obtained from the different fiber tracking algorithms are reported in the following. Only results of the SD STREAM and iFOD2 algorithms are reported, since the FACT algorithm failed to generate any streamline in any of the patients. As example, a facial nerve reconstruction without the use of exclusion ROI is presented for the first patient, to underline how important was to exclude areas not involved in the passage of the nerve. A comparison between the SD STREAM

results and those of iFOD2, obtained applying the total acquisition protocol, is made only for the second patient. The graphical comparison between results of different protocols is illustrated as an example only for the fifth patient. The color legend of the streamlines is that reported in Figure 2.5.

### Patient 1

This patient was affected by right VS. From the intraoperative evaluation, the course of the facial nerve resulted straight from the brainstem to the auditory internal canal. It originated in the antero-inferior position with respect to the VS and it was in the antero-medial position during its passage in the cisternal tract. The reconstruction of the FN with iFOD2 algorithm confirmed the course of the nerve as recorded during the surgery. Figure 3.2 shows the resulting fibers obtained using the iFOD2 algorithm, without the aid of additional masks to exclude the tracts reconstructed outside the regions of interest. The goal of this image is to underline how difficult it would be the reconstruction of the FN without providing additional masks to help tracking algorithms to isolate the fibers related to the FN only. Figure 3.3 displays the FN reconstructed with iFOD2 algorithm in the healthy part. The 3D reconstruction of FN in the right unhealthy part is shown nearby the tumor mass in Figure 3.4. Figure 3.5 shows an intraoperative visualization of the FN after the removal of the tumor.

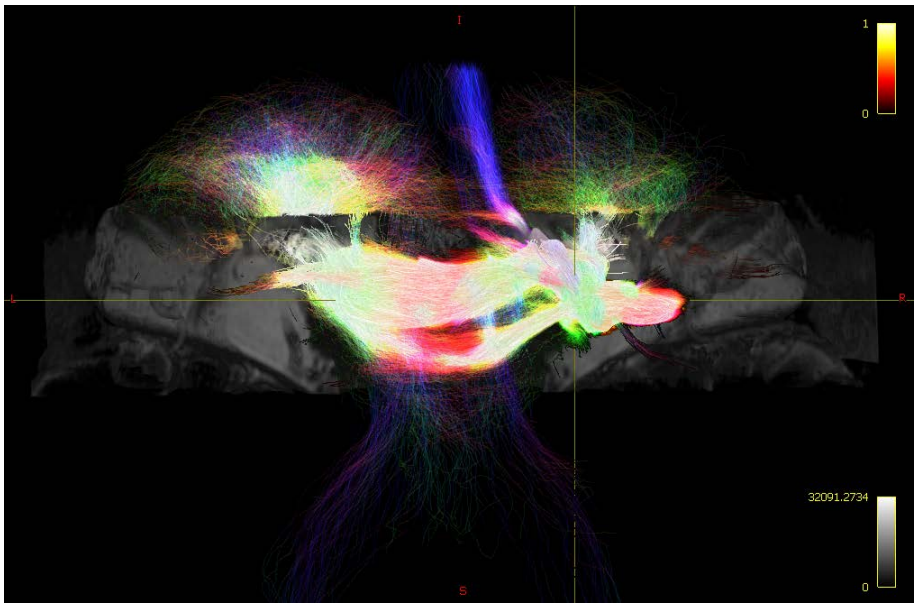


Figure 3.2: Fibers reconstruction with iFOD2 algorithm, without using exclusion masks. The streamlines are displayed superposed on the high resolution T2w image. The point where the yellow straight lines cross indicates the position of passage of the FN. This latter is not distinguishable, given the large number of reconstructed fibers.

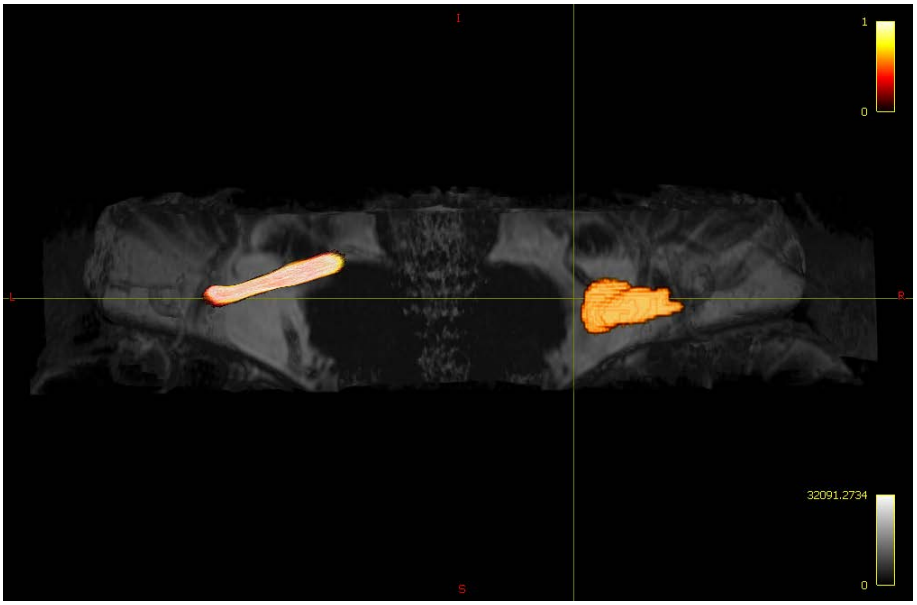


Figure 3.3: Reconstruction of FN in the left healthy part using the iFOD2 algorithm. The course of the healthy FN results straight and well defined, as expected. The segmented tumor mass is represented on the right in red scale.

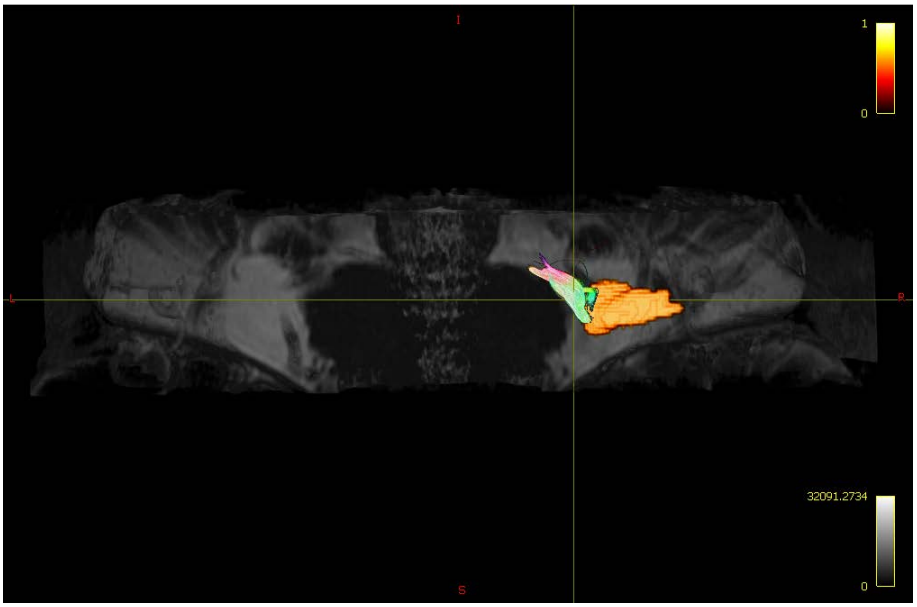


Figure 3.4: Reconstruction of FN in the right unhealthy part using the iFOD2 algorithm. The point where the yellow straight lines cross indicates the position of passage of FN in the antero-medial portion of the tumor capsule. The segmented tumor mass is represented on the right in red scale.

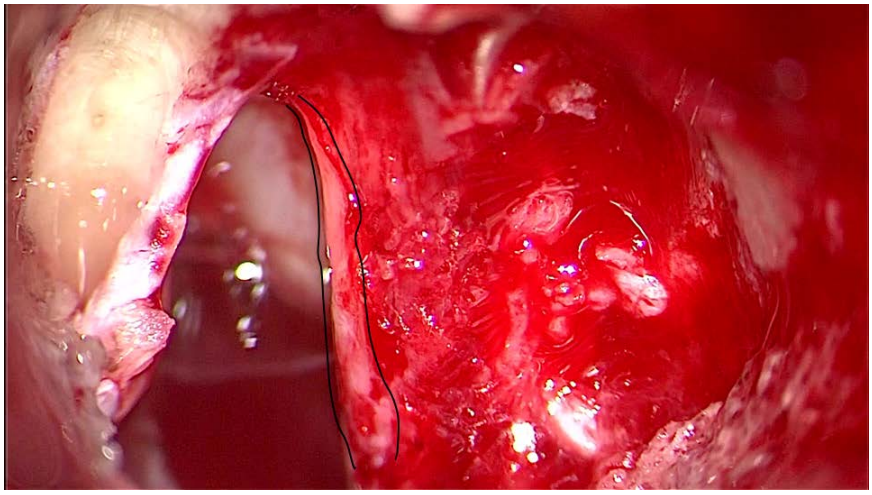

Figure 3.5: Intraoperative image of the FN after the removal of the tumor mass. The nerve is between the two black lines.

### Patient 2

The VS was observed in the right part. The FN originated in antero-inferior position with respect to the VS location and then it moved to the antero-medial part of the VS. The facial and cochlear nerves resulted very close to each other, in fact the tumor dislocated both nerves and compressed them.
Also for this patient the FN reconstruction, obtained with the iFOD2 algorithm and shown in Figure 3.6, confirmed the intraoperative evaluation.
In Figure 3.7 the FN reconstruction obtained with the SD STREAM algorithm is also displayed. This figure highlights that this latter method is less precise and generates fewer fibers than the iFOD2, as explained in section 2.5. Figure 3.8 shows an intraoperative image in which the FN after tumor removal is clearly visible after tumor removal.

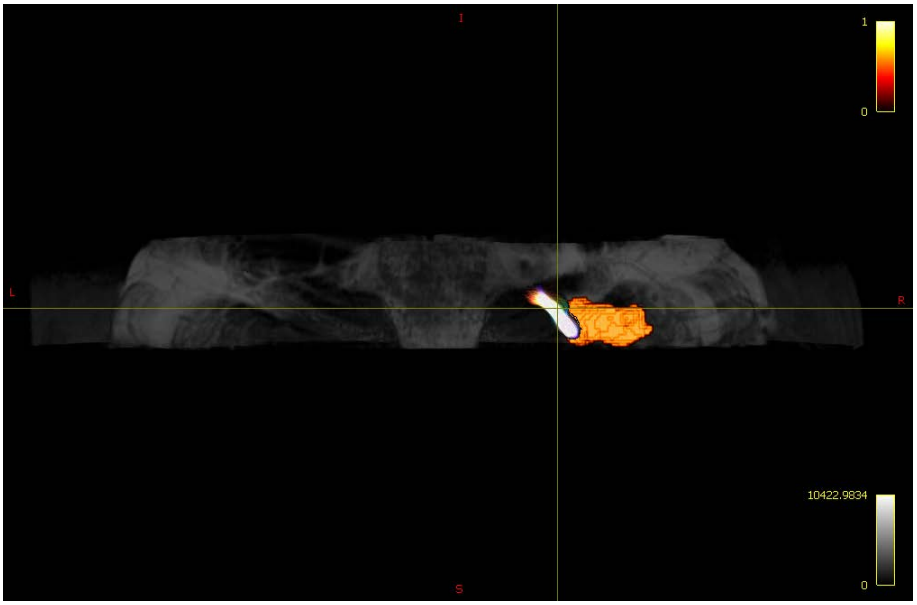


Figure 3.6: Reconstruction of FN in the right unhealthy part using the iFOD2 algorithm. The point where the yellow straight lines cross indicates the position of passage of FN in the antero-medial portion of the tumor capsule. The segmented tumor mass is represented on the right in red scale.

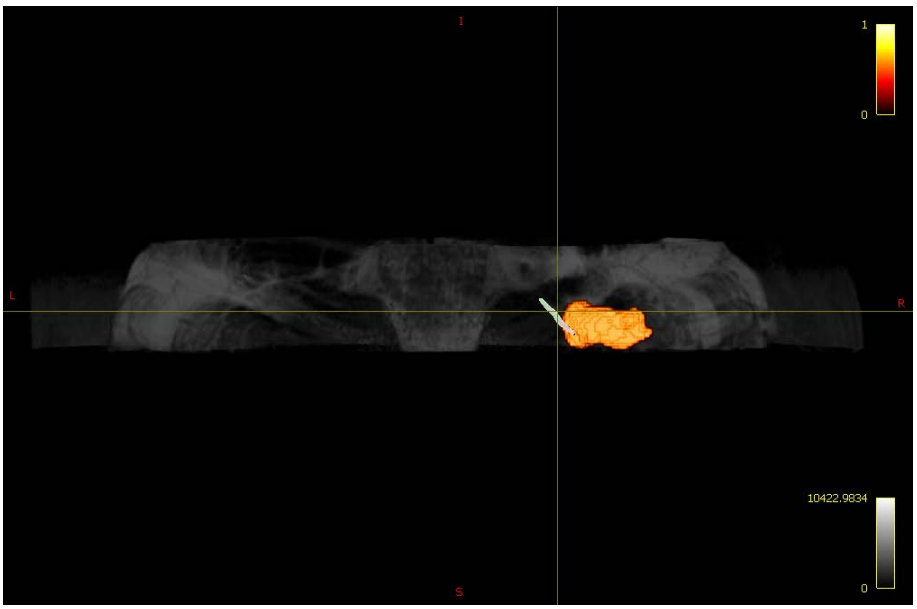


Figure 3.7: Reconstruction of FN in the right unhealthy part using the SD STREAM algorithm. The point where the yellow straight lines cross indicates the position of passage of FN in the antero-medial portion of the tumor capsule. As compared to the reconstruction in Figure 3.6, the SD STREAM algorithm generates fewer fibers and seems less accurate.

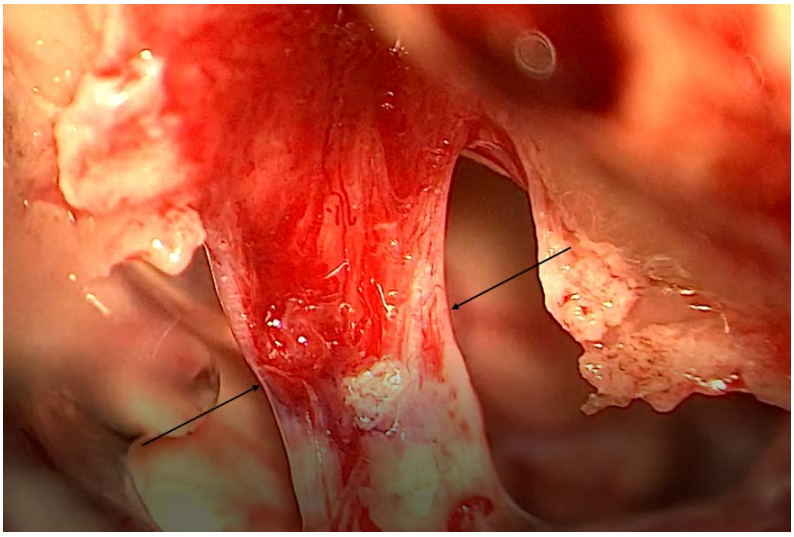

Figure 3.8: Intraoperative image of the FN after the removal of the tumor mass. The nerve is indicated between the black arrows.

### Patient 3 - limit case

In this patient the tumor was found on the right part. This patient was labeled as "limit case" because the FN was divided into many and very thin fibers that were spread on the posterior part of the tumor. In this position, the FN was the first thing that the surgeon encountered before reaching the tumor. The localization of these fibers by the surgeon took a long time and, without the aid of electrostimulation, it would have been impossible to recognize that those fibers were part of the facial nerve. Once the nerve was recognized, the surgeons had to decide whether to remove the tumor, thus damaging the FN, or to not excise the tumor mass. After reaching a consensus with the patient's family, the surgeon removed the tumor and the FN had to be artificially reconstructed. This led to a definitive paralysis on the right part of the face of the patient. The iFOD2 algorithm reconstructed a very different course of the FN compared to those of the previous patients (Figure 3.9). This particular distribution of the fibers of the FN on the tumor capsule was confirmed by intraoperative results. In this particular situation, if the surgeons knew in advance that the course of the reconstructed FN resulted in a set of fibers distributed on the tumor in that particular location, they would have planned the surgery differently. Moreover, the patient would have been informed in advanced of the complexity of the surgery and of the associated risks and possible outcome. Figure 3.10 shows an intraoperative image of the posterior part of the tumor.

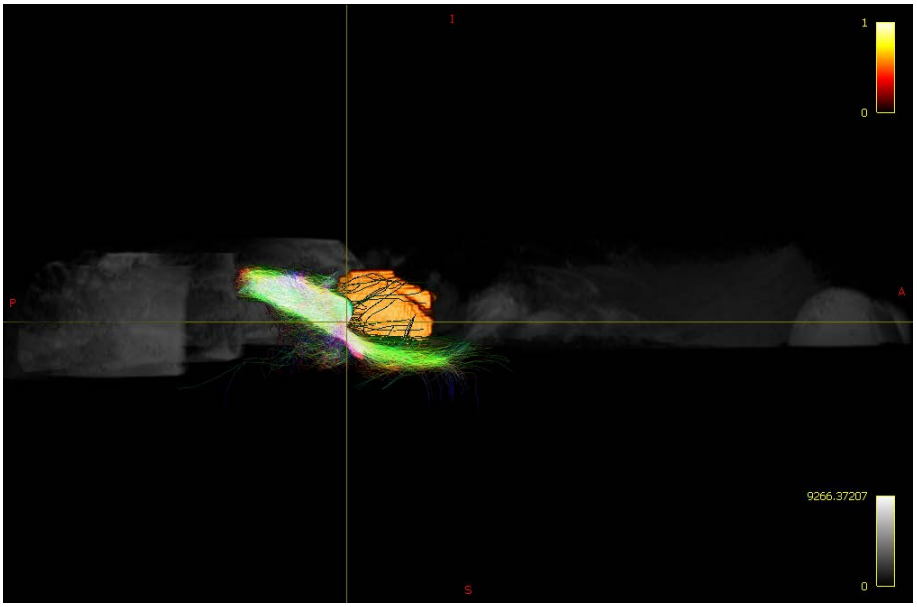


Figure 3.9: Reconstruction of FN in the right unhealthy part using the iFOD2 algorithm. The fibers result in a very confused configuration on the posterior part of the tumor capsule. The segmented tumor mass is represented on the left in red scale.

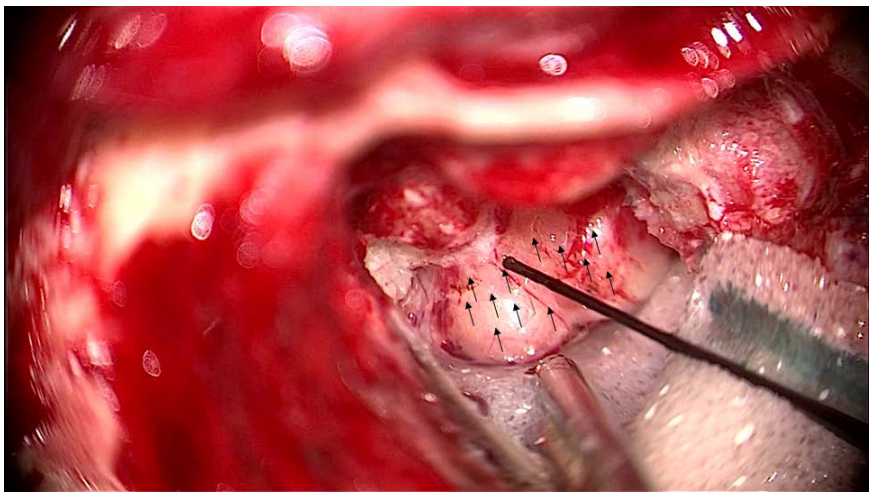

Figure 3.10: Intraoperative image of the posterior part of the tumor wrapped by the fibers of the FN. Since the nerve was found to consist of a set of tiny fibers, these are represented in the figure by the black arrows. On the right part of the image the probe that was used for electrostimulation is also visible.

### Patient 4 - limit case

The patient was affected by right VS. The FN originated in the antero-medial face of the tumor, in a direction perpendicular to that of the vestibular nerve. This configuration represented a second limit case, since the facial nerve usually has a course parallel to the vestibular nerve. In the cisternal tract the FN moved on the antero-superior part of the tumor. Since the maximum curvature angle allowed for the iFOD2 algorithm was set at 45°, the reconstructed FN course was not completely faithful to the intraoperative results. However, the algorithm was able to reconstruct an approximate course of the FN. The FN reconstruction is shown in Figure 3.11, whilst Figure 3.12 shows the FN after the tumor removal.

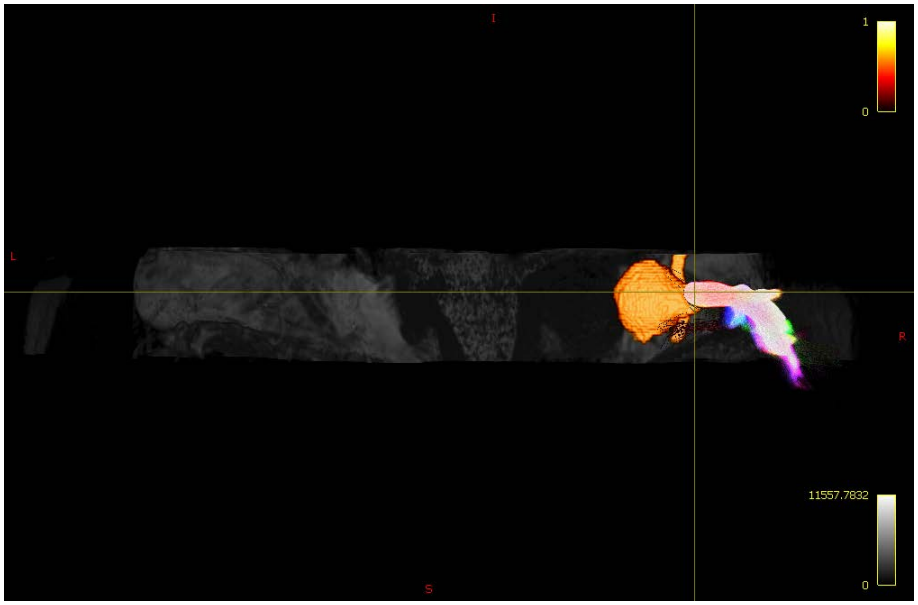


Figure 3.11: Reconstruction of FN in the right unhealthy part using the iFOD2 algorithm. The course of the nerve shows a very high angle of curvature, which, although not exactly reflecting the intraoperative findings, provides a good approximation. The segmented tumor mass is represented on the right in red scale.

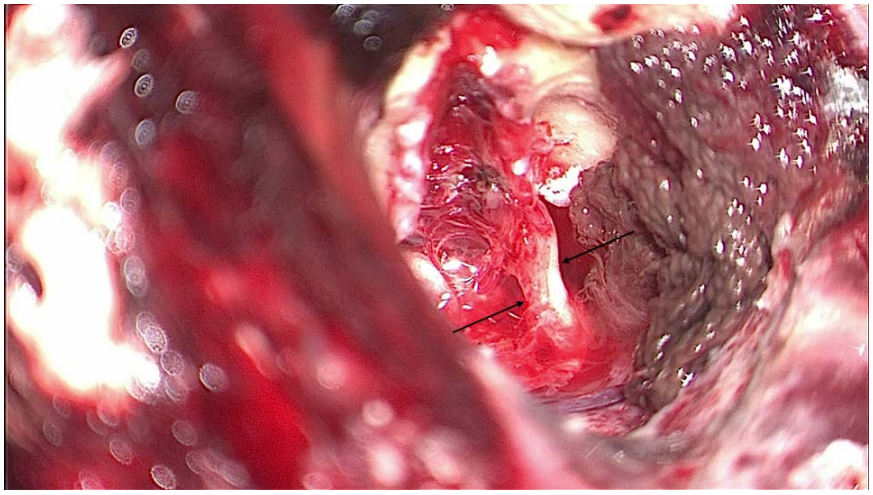

Figure 3.12: Intraoperative image of the FN after the removal of the VS. The two black arrows point to the location of the FN.

### Patient 5

In this patient the VS was observed in the left part. The FN originated antero-medially with respect to the tumor and then it moved to antero-superior position. The course of FN observed during the surgery was a typical course. The iFOD2 algorithm indeed reconstructed the FN in a very accurate way, as shown in Figure 3.13. The qualitative comparison between the different reduced protocols applied with the iFOD2 algorithm is presented for this patient as illustrative example. The following considerations on reduced protocols are valid also when the SD STREAM algorithm is applied, but taking into account that the reconstructions become worse. In Figure 3.14 the FN reconstruction by applying the protocol with a single b-value equal to 300s/mm$^2$ is displayed. This reconstruction shows that by using a mono-shell DTI protocol with a low b-value, the reconstructed fibers are fewer if compared with those of the total protocol and the curvature angles of the fibers are not very physiological. Furthermore, for this patient the reconstructed nerve appears to consist of two different fiber populations that are joined together by the algorithm. In Figure 3.15 the results of the single-shell DTI protocol with b-value equal to 1000s/mm$^2$ are displayed. The same considerations can be made as in the previous case. Instead, by using only a high b-value equal to 2000s/mm$^2$, more tracts are generated and the reconstruction seems to provide interesting results. It is worth noting, however, that high b-values lead to diffusion images with low SNR thus increasing the chance to get false positives. The last tested reduced protocol was that obtained by reducing the diffusion directions to half of the originals. With this reduced protocols, the reconstruction the reconstruction of FN, displayed in Figure 3.17, is not physiological, since it is not plausible that the FN course makes such high curvature angles in the cisternal tract. In Figure 3.18 the FN observed during the surgery, after the tumor removal, is shown.

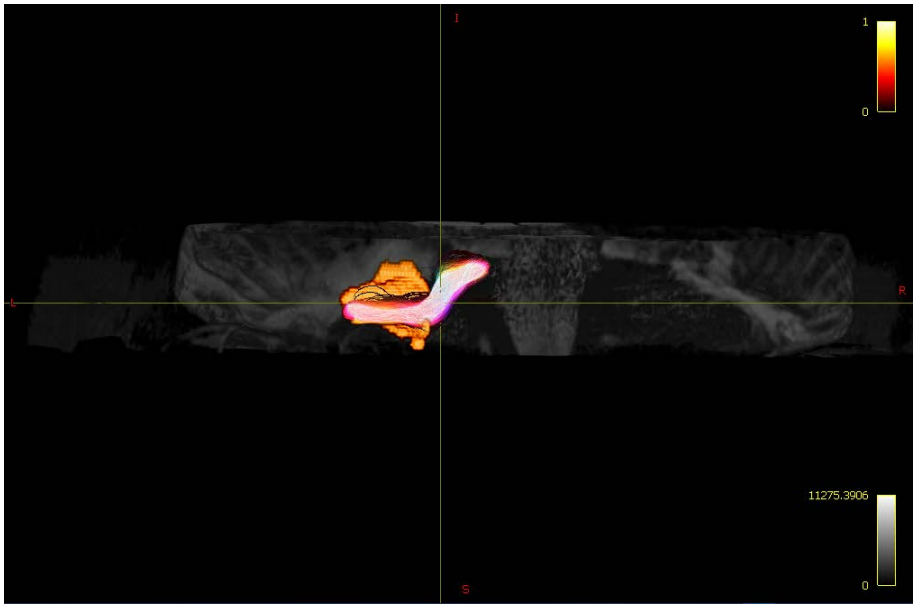


Figure 3.13: Reconstruction of FN in the left unhealthy part using the iFOD2 algorithm applied to the total protocol. The point where the yellow straight lines cross indicates the position of passage of FN in the antero-superior portion of the tumor capsule. The segmented tumor mass is represented on the right in red scale.

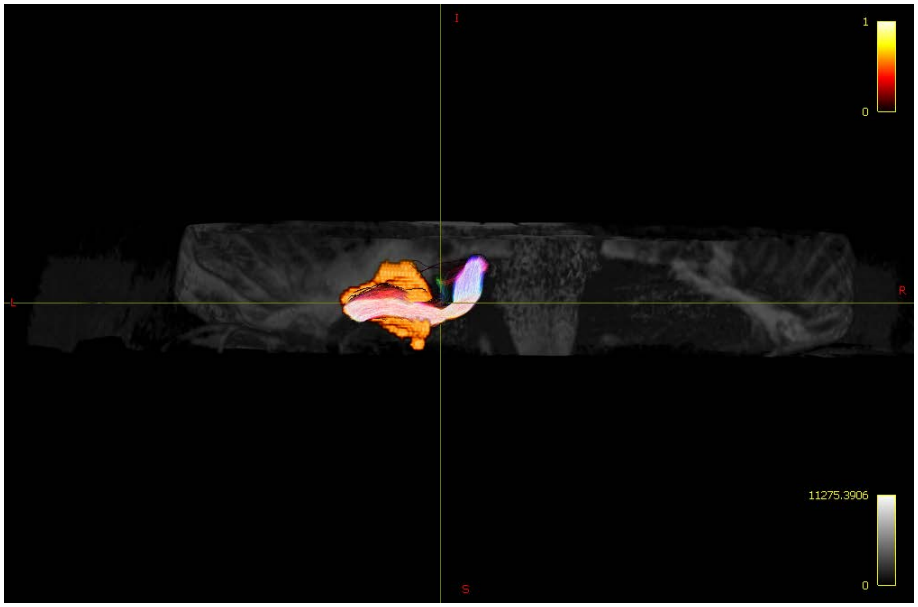


Figure 3.14: Reconstruction of FN in the left unhealthy part using the iFOD2 algorithm applied to the mono-shell DTI protocol with b-value equal to 300s/mm$^2$ and the iFOD2 method. The course of the FN results non-physiological if compared to that of the total protocol.

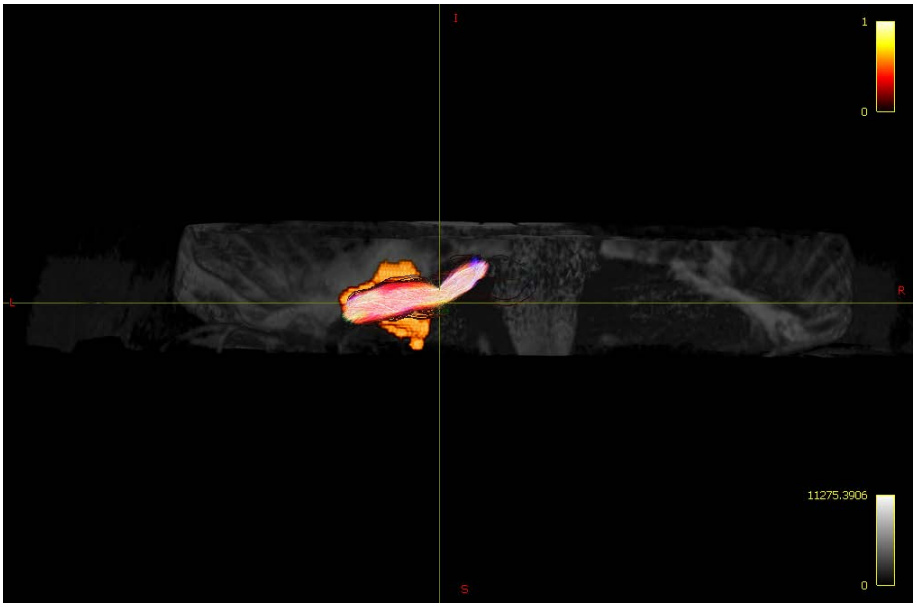


Figure 3.15: Reconstruction of FN in the left unhealthy part using the iFOD2 algorithm applied to the mono-shell DTI protocol with b-value equal to 1000s/mm$^2$ and the iFOD2 method. The angles of curvature of the fibers highlight a non-physiological course of the FN.

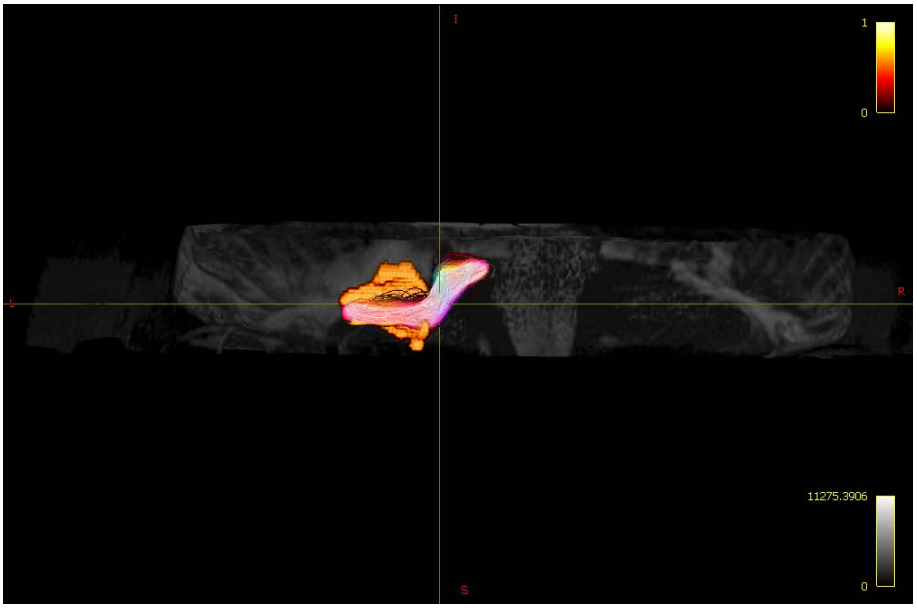


Figure 3.16: Reconstruction of FN in the left unhealthy part using the iFOD2 algorithm applied to the mono-shell DTI protocol with b-value equal to 2000s/mm$^2$ and the iFOD2 method. The tracts generated are similar to those of the total protocol, but it is likely that many tracts coincide with false positives.

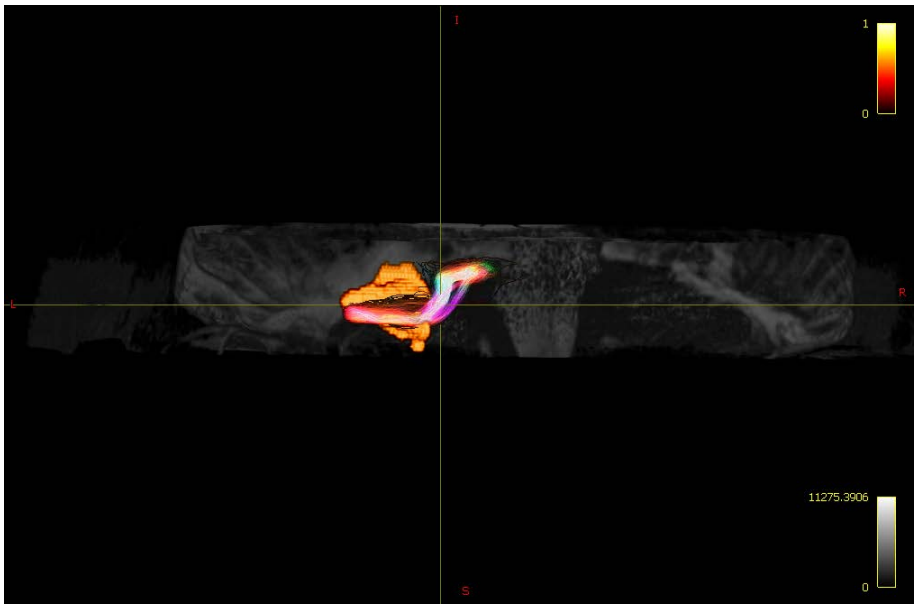


Figure 3.17: FN reconstruction by applying the half protocol and the iFOD2 method. The course of FN is not physiological if compared with that found with the total protocol.

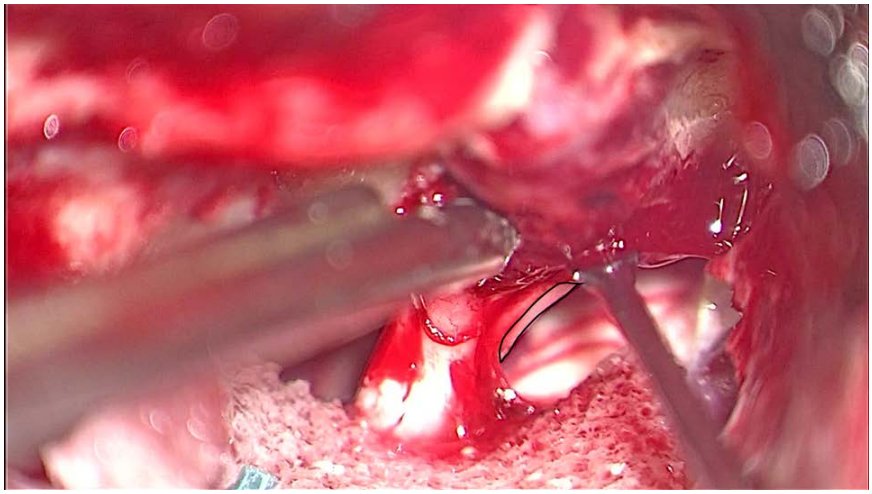

Figure 3.18: Intraoperative image of the FN after the removal of the VS. The nerve is that contoured in black.

## 3.3 Quantitative analysis

### 3.3.1 Total vs. reduced protocols

The scores assigned to the total acquisition protocol and to the reduced ones (see subsection 2.9.1) are reported for both probabilistic tracking methods in table 3.4 for iFOD2 algorithm and in 3.5 for the SD STREAM one. The scores were assigned by the three observers and given on the basis of the goodness of the facial nerve reconstruction, evaluated by comparing it with the real course of the nerve as found in the video recorded during the surgery. The results show that the iFOD2 algorithm applied to the total protocol seems the most appropriate to carry out the reconstruction of FN, followed by the SD STREAM algorithm always applied to the total protocol. This suggests that the total protocol guarantees the possibility to find more fibers and with less false positives than the protocol using the higher b-value (2000s/mm$^2$) only and reconstructs more physiological curvature angles than the protocols with low b-values.

| | TOTAL | b=300 | b=1000 | b=2000 | HALF |
|---|---|---|---|---|---|
| Patient 1 | **3** | 1 | 2 | 1 | 2 |
| Patient 2 | **3** | 1 | 2 | **3** | **3** |
| Patient 3 | 1 | 0 | 1 | 1 | 0 |
| Patient 4 | 1 | 0 | 1 | 0 | 0 |
| Patient 5 | **3** | 0 | 0 | 2 | 0 |

Table 3.4: Sum of the scores given by three independent observers to the total and reduced protocols tested with the iFOD2 tracking algorithm. Each observer could give a score of 1 if the reconstructed FN had a pattern similar to the one of the video or of 0 otherwise. The score equal to 3 represents the unanimous vote of the observers and therefore a complete success in reconstructing the FN course.

| | TOTAL | b=300 | b=1000 | b=2000 | HALF |
|---|---|---|---|---|---|
| Patient 1 | **3** | 0 | 1 | 2 | 0 |
| Patient 2 | **3** | 0 | 0 | **3** | 0 |
| Patient 3 | 0 | 0 | 0 | 0 | 0 |
| Patient 4 | 1 | 0 | 1 | 1 | 0 |
| Patient 5 | 0 | 0 | 0 | 0 | 0 |

Table 3.5: Sum of the scores given by three independent observers to the total and reduced protocols tested with the SD STREAM tracking algorithm. Each observer could give a score of 1 if the reconstructed FN had a pattern similar to the one of the video or of 0 otherwise. The score equal to 3 represents the unanimous vote of the observers and therefore a complete success in reconstructing the FN course.

### 3.3.2 Metrics comparison

Since the previous analysis suggested that the most reliable method for FN reconstruction is the iFOD2, the diffusion indices AD, ADC, FA and RD were evaluated only for this method. Figures 3.19, 3.20, 3.21, 3.22 and 3.23 report the four diffusion metrics (AD, ADC, FA and RD) for each of the five different protocols in each of the 5 patients. These figures show that for patients 1, 2 and 5 all metrics show considerable variations between the different protocols, with a similar pattern for all metrics. Patient 3 and 4, instead, our case limits, show a different pattern across protocols among the metrics. In particular, FA seems to show an opposite behavior compared to the other three metrics. Finally, in Figure 3.24 a further comparison between diffusion metrics obtained in the five patients when adopting the total protocol is displayed. The results show that patient 3, one of our case limit, presents values in all four metrics far away from the values obtained in the other patients, above all for FA metric. Patient 4, instead, the other case limit, does not seem to behave differently than the other patients.

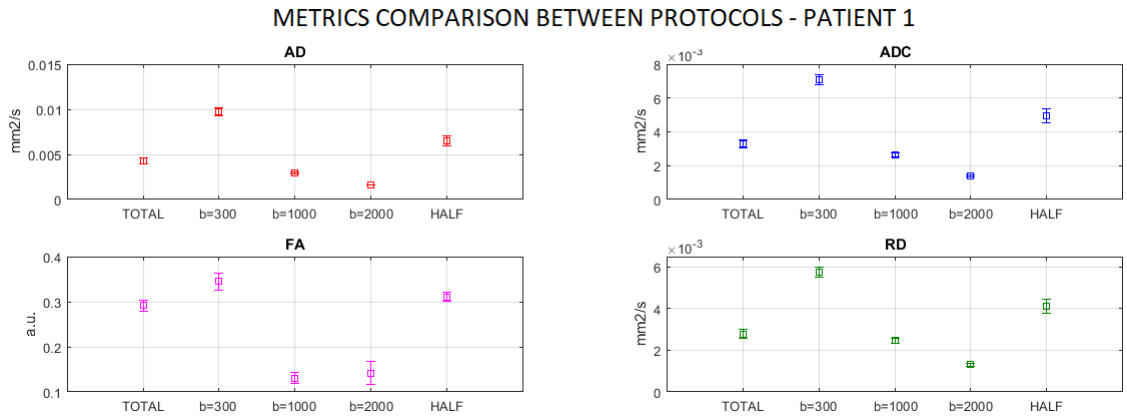


Figure 3.19: Diffusion metrics comparison between the five protocol tested in patient 1. The mean value of the metrics is represented by the square and the standard deviation by the error bar.

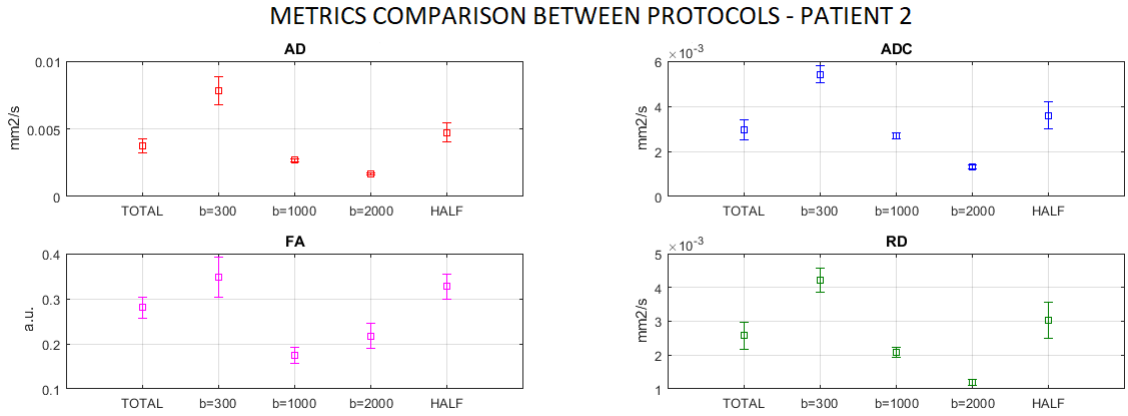


Figure 3.20: Diffusion metrics comparison between the five protocol tested in patient 2. The mean value of the metrics is represented by the square and the standard deviation by the error bar.

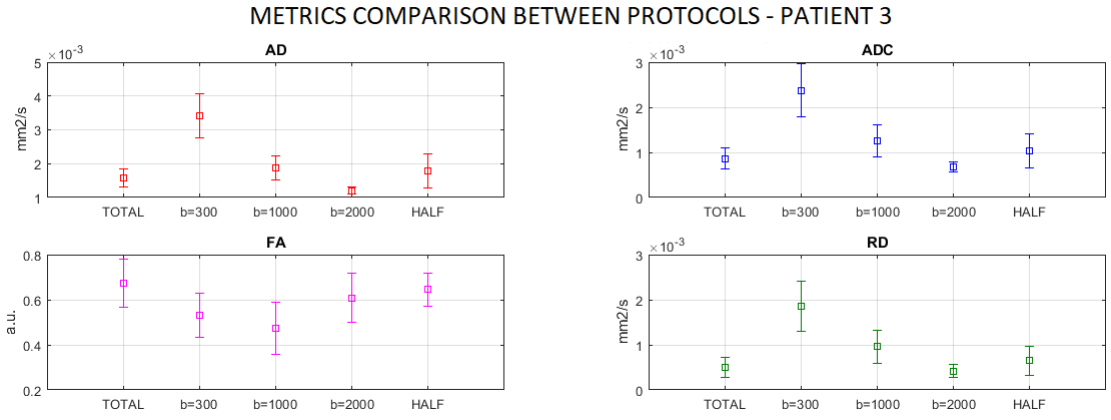


Figure 3.21: Diffusion metrics comparison between the five protocol tested in patient 3. The mean value of the metrics is represented by the square and the standard deviation by the error bar.

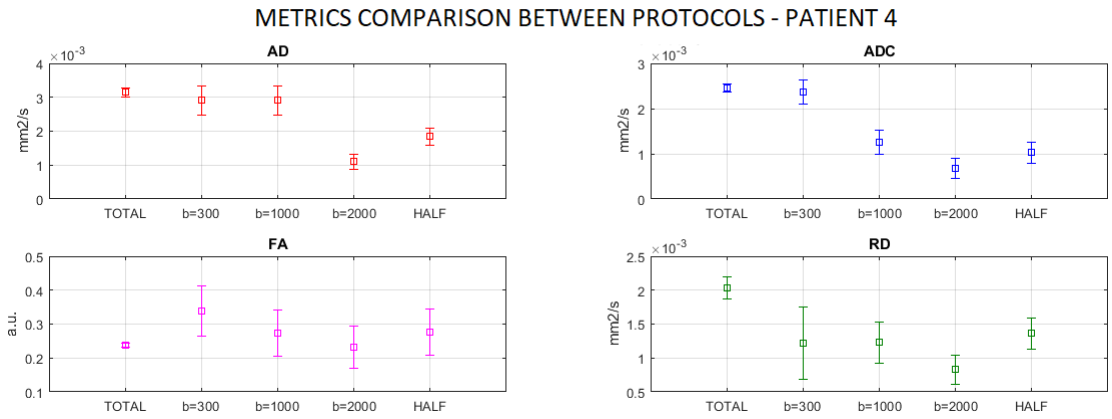


Figure 3.22: Diffusion metrics comparison between the five protocol tested in patient 4. The mean value of the metrics is represented by the square and the standard deviation by the error bar.

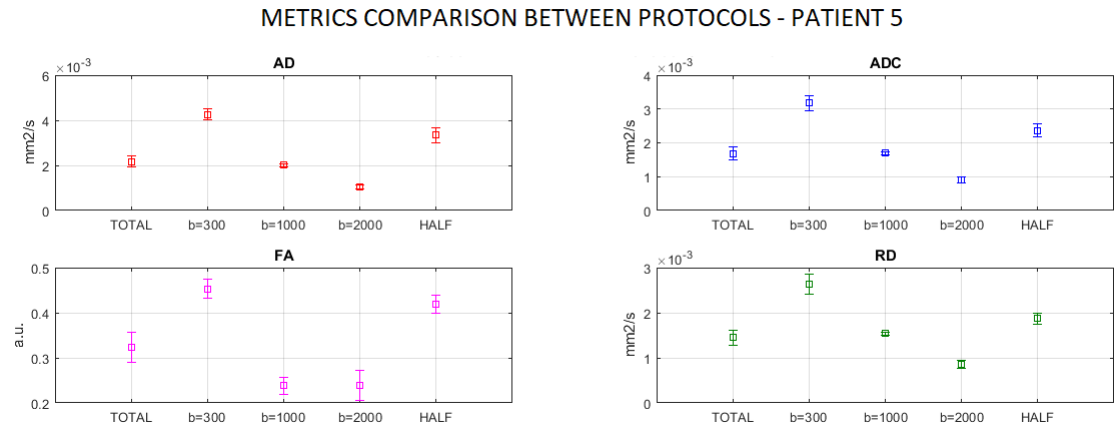


Figure 3.23: Diffusion metrics comparison between the five protocol tested in patient 5. The mean value of the metrics is represented by the square and the standard deviation by the error bar.

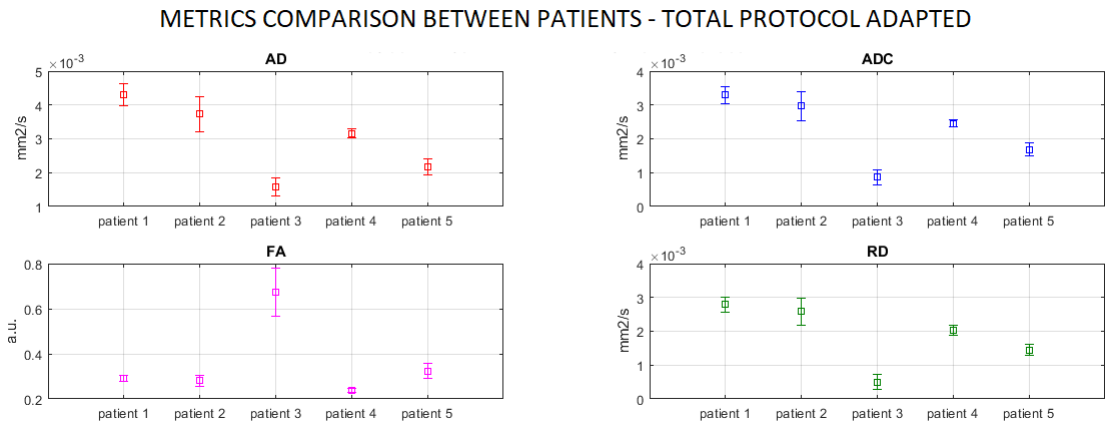


Figure 3.24: Diffusion metrics comparison between the five analyzed patients when using the total acquisition protocol. The mean value of the metrics is represented by the square and the standard deviation by the error bar.

# Chapter 4

# Discussion

## 4.1 Qualitative analysis

The qualitative analysis performed with a team of experienced physicians showed that in three of the five patients, the FN reconstructions confirmed what was seen during the surgery. Instead, for the two cases of the third and fourth patients, described as limit cases, the reconstructions, although not completely faithful to the intraoperative findings, have anyway allowed to evaluate the feasibility of the use of probabilistic fiber tracking algorithms even where the FN takes very complex configurations due to the presence of the tumor that dislocates it. For these last two critical cases, having known before the surgery that the FN assumed such a complex configuration, would have helped the surgeons to plan the operation in a better way, making important decisions before the surgery. Nevertheless, even in the other three cases, in which the facial nerve was detected more easily during the surgery, the pre-operative DTI fiber tracking reconstructions could have helped the best planning of the surgery. Moreover, they could have reduced the duration of the surgery, thanks to a faster localization of the course of the facial nerve.

## 4.2 Quantitative analysis

### 4.2.1 Total vs. reduced protocols

The analysis of fiber tracking results obtained from the total and the reduced protocols suggested that the use of low b-values leads to reconstruct diffusion images with high SNR but, at the same time, it only manages to solve lower and less physiological curvature angles. The use of only high b-values, instead, leads to a higher number of false positives in the reconstructed fibers, but manages to solve larger curvature angles.
The conclusion that can be drawn from the comparison between protocols is that only the total multi-shell DTI protocol is able to give physiologically plausible results, while none of the reduced protocols provides results reliable enough to be

employed in clinical practice. Therefore, the total acquisition time for an accurate reconstruction of the facial nerve can not be reduced to less than 40 minutes.

### 4.2.2 Metrics comparison

Figures 3.19, 3.20, 3.21, 3.22 and 3.23 reported in subsection 3.3.2 show that all metrics present considerable variations between the different protocols in all patients. The most interesting metric seems to be FA, which has a different behavior in the two case limit patients compared to the other three easier patients. For this metric, remembering that FA values less than 0.18 are considered to describe a diffusive isotropic process, the following observations can be made regarding the figures mentioned above:

1. Patient 1: the mono-shell protocols with b=1000s/mm$^2$ or b=2000s/mm$^2$ emphasize an isotropic feature of the reconstructed fibers.
   This is in agreement with the fiber tracking results where, for these two protocols, the origin of the FN seemed to be not differentiated with respect to that of the cochlear nerve. Therefore, remembering that the reported FA values are a mean of those obtained from the maps constructed from the tracking results, even if a few low FA values are present, they can lead to a much lower average value.

2. Patient 2: the same considerations as in the previous case can be made regarding the two mono-shell protocols.

3. Patient 3: the values of FA suggest a high degree of anisotropy, hence the expected results would be a single well-oriented fiber package.
   However, considering the intraoperative results, as explained in the previous section, the nerve in this patient was divided into many fibers. The FA values of the five protocols are therefore untrustworthy as already underlined by the scores given to fiber tracking results for this patient in Table 3.4.

4. Patient 4: the FA values underline a degree of low anisotropy that is not in agreement with the straight course of FN, although in this patient FN was found to be perpendicular to the vestibular nerve.
   These values reflect an inaccurate fiber reconstruction.

5. Patient 5: the values of FA are very different between protocols, especially among single-shell protocols.
   These results confirm the scores in Table 3.4, except for the mono-shell protocol with b=2000s/mm$^2$. This could be due to the fact that some fibers correspond to false positive and are reconstructed randomly without following the preferential direction followed by other fibers.

The metrics comparison between patients reported in Figure 3.24 shows that all the diffusion indices of patient 3, one of the two limit cases, deviate from the

average of the other values, especially for the FA value.
This could be due to the fact that the large number of fibers that are reconstructed in this patient have very discordant directions, as underlined by the wide standard deviation of the FA value, which can range from about 0.6 to 0.8.

# Chapter 5

# Conclusions

The results of this thesis showed that DTI fiber tracking can be a powerful aid for a better presurgical planning of vestibular schwannoma removal. Applying fiber tractography to evaluate the facial nerve course is not an easy task, since it is very close to the cochlear nerve. Furthermore, cranial nerves regions are at low SNR and fibers can present complex patterns. For these reasons the analysis of fiber tracking results obtained with the four DTI sub-protocols showed that the use of low b-values does not manage to solve high fiber curvature angles, whereas high b-values lead to a high number of false positive. Therefore, only the total multi-shell DTI protocol provided results reliable enough to be employed in clinical practice. The analysis also demonstrated that only probabilistic algorithms manage to solve complex fibers patterns and can give a faithful reconstruction of the course of the facial nerve. Among the tested fiber tracking algorithms, the deterministic method (FACT) was discarded, since it failed to generate any streamline in any of the patients. The SD STREAM algorithm, being in its mathematical description less precise in evaluating the distribution of the fibers, was not always able to reconstruct streamlines for the nerve, although providing, when the reconstruction was successful, meaningful results. The iFOD2 algorithm resulted to be the most suitable for FN reconstruction. The SD STREAM method could therefore be used to support the validation of the iFOD2 results. The qualitative validation of results carried out with a team of experienced physicians showed that the multi-shell DTI protocol, with the anatomical help of the standard pre-surgical MR sequences, was able to reconstruct the course of facial nerve in a physiologically way and faithful to the intraoperative findings in 3 of the 5 patients. In two cases, described by the surgeons as limit cases, the reconstructions, although not completely faithful to the intraoperative findings, have anyway allowed to evaluate the feasibility of the use of probabilistic fiber tracking algorithms. For these two cases, having informed the surgeons before the surgery of the complex pattern of the fibers present nearby the tumor, would have allowed to better plan the surgery and to inform the patients about the possible post-surgery complications. The faithful reconstruction of the facial nerve has been made possible only by providing additional anatomical information to the tracking algorithms. Therefore, the cooperation between experienced physicians

and the bioengineering team was essential for the success of this project.
The results of this thesis will promote further steps in the project: firstly the application of this DTI fiber tracking pipeline on a cohort of healthy controls matched for sex and age with a cohort of unhealthy patients and secondly the loading of the reconstructed nerve courses on the neuronavigation system that surgeons use as aid during the surgery. This additional real-time and patient-specific information should decrease the duration of the surgery, help the surgeons to preserve the facial nerve, and improve patients' outcome.

# Bibliography


[1] "I NEURINOMI DELL'ACUSTICO". October 2008. *Clinica Neurochirurgica.* http://www.neurochirurgiafirenze.it/neurinoma_acustico.html

[2] BANCIU E.; ATTYE A.; MENDOZA C.; LAMALLE L.; TROPRES I.; TAHON F.; BOUBAGRA K.; KRAINIK A.; GRENOBE; MEYLAN; LA TRONCHE; *The inner imaging anatomy with 3T MRI new sequences: A comprehensive update*, European Society of Radiology, 2014.

[3] DAROFF R.B.; JANKOVIC J.; MAZZOTTA J.C.; POMEROY S.L.; *Bradley's Neurology in Clinical Practice*, Elsevier, 2016, $7^{th}$ edition, vol. I, p.596.

[4] "Vestibular Schwannoma (Acoustic Neuroma) and Neurofibromatosis". *NIH.* No.99-580. November 2015. https://www.nidcd.nih.gov/health/vestibular-schwannoma-acoustic-neuroma-and-neurofibromatosis

[5] "Acoustic neuroma". *MAYO CLINIC.* https://www.mayoclinic.org/diseases-conditions/acoustic-neuroma/diagnosis-treatment/drc-20356132

[6] "Neurinoma acustico-Schwannoma vestibolare". *Tanzariello.* 2016. www.tanzariello.it/index.php/orecchio/patologia-orecchio/patologie-del-sistema-vestibolare-centrale/44-studio-prof-a-tanzariello/orecchio/patologia/patologia-del-sistema-nervoso-centrale-vertigini-da-causa-centrale/quadri-clinici-otoneurologici-delle-lesioni-dell-angolo-ponto-cerebellare-e-della-fossa-cranica-posteriore/871-neurinoma-acustico-schwannoma-vestibolare

[7] RAJAGOPALAN V.; JIANG Z.; STOJANOVIC-RADIC J.; YUE G.H.; PIORO E.P.; WYLIE G.R.; DAS A.; *A Basic Introduction to Diffusion Tensor Imaging Mathematics and Image Processing Steps*, Brain Disorders & Therapy, vol.6, 2017.

[8] JOHANSEN-BERG H.; BEHRENS T.E.J.; *Diffusion MRI: From Quantitative Measurement to In vivo Neuroanatomy*, Elsevier, 2009, $2^{nd}$ edition, p.7-8.

[9] MORI S.; TOURNIER J-D.; *Introduction to Diffusion Tensor Imaging*, Elsevier, 2014, $2^{nd}$ edition.

[10] ROSENBLOOM M.; SULLIVAN E.V.; PFEFFERBAUM A.; *Using Magnetic Resonance Imaging and Diffusion Tensor Imaging to Address Brain Damage in Alcoholics*, National Institute on Alcohol Abuse and Alcoholism, vol.27, 2003, p.146-152.

[11] HAHN E.L.; *Spin echoes*, Physical Review, vol.80, 1950.

[12] CARR H.Y.; PURCELL E.M:; *Effects of Diffusion on Free Precession in Nuclear Magnetic Resonance Experiments*, Physical Review, vol.94, 1954.

[13] TORREY H.C.; *Bloch equations with diffusion terms*, Physical Review, vol.104, 1956.

[14] STEJSKAL E.O.; TANNER J.E.; *Spin Diffusion Measurements: Spin Echoes in the Presence of a Time-Dependent Field Gradient*, Journal of Chemical Physics, vol.42, 1965.

[15] Hammer, Mark. "MRI Physics: Diffusion-Weighted Imaging". http://xrayphysics.com/dwi.html

[16] MORI S.; ZHANG J.; *Principles of Diffusion Tensor Imaging and Its Applications to Basic Neuroscience Research*, *Neuron*, Elsevier, vol.51, 2006, p.527-539.

[17] BURDETTE J.H.; DURDEN D.D.; ELSTER A.D.; YEN Y.F.; *High b-Value Diffusion-Weighted MRI of Normal Brain*, Journal of Computer Assisted Tomography, vol.25, 2001, p.515-519.

[18] IHN Y.K.; HWANG S.S.; PARK Y.H.; *Acute Marchiafava-Bignami Disease: Diffusion-Weighted MRI in Cortical and Callosal Involvement*, Yonsei Med J, vol.48, 2007.

[19] PRADOS F.; BOADA I.; PRATS-GALINO A.; MARTIN-FERNANDEZ J.A.; FEIXAS M.; BLASCO G.; PUIG J.; PEDRAZA S.; *Analysis of New Diffusion Tensor Imaging Anisotropy Measures in the Three-Phase Plot*, Journal of Magnetic Resonance Imaging, vol.31, 2010, p.1435-1444.

[20] PIERPAOLI C.; BASSER P.J.; *Toward a Quantitative Assessment of Diffusion Anisotropy*, Magnetic Resonance in Medicine, vol.36, 1996.

[21] DONG Q.; WELSH R.C.; CHENEVERT T.L.; CARLOS R.C.; MALY-SUNDGREN P.; GOMEZ-HASSAN D.M.; MUKHERJI S.K.; *Clinical Applications of Diffusion Tensor Imaging*, Journal of Magnetic Resonance Imaging, vol.19, 2004, p.6-18.

[22] BASSER P.J.; PAJEVIC S.; PIERPAOLI C.; DUDA J.; ALDROUBI A.; *In Vivo Fiber Tractography Using DT-MRI Data*, Magnetic Resonance in Medicine, vol.44, 2000, p.625-632.

[23] MORI S.; CRAIN B.J.; CHACKO V.P.; ZIJL M.P.C.; *Three-Dimensional Tracking of Axonal Projections in the Brain by Magnetic Resonance Imaging*, Annals of Neurology, vol.45, 1999, p.265-269.

[24] MUKHERJEE P.; BERMAN J.I.; CHUNG S.W.; HESS C.P.; HENRY R.G.; *Diffusion Tensor MR Imaging and Fiber Tractography: Theoretic Underpinnings*, American Journal of Neuroradiology, vol.29, 2008, p.632-641.

[25] TOURNIER J.D.; MORI S.; LEEMANS A.; *Diffusion Tensor Imaging and Beyond*, Magnetic Resonance in Medicine, vol.65, 2011, p.1532-1556.

[26] JENSEN J.H.; HELPERN J.A.; RAMANI A.; LU H.; KACZYNSKI K.; *Diffusional kurtosis imaging: the quantification of non-gaussian water diffusion by means of magnetic resonance imaging*, Magnetic Resonance in Medicine, vol.53, 2005, p.1432-1440.

[27] NIENDORF T.; DIJKHUIZEN R.M.; NORRIS D.G.; VAN LOOKEREN CAMPAGNE M.; NICOLAY K.; *Biexponential diffusion attenuation in various states of brain tissue: implications for diffusion-weighted imaging*, Magnetic Resonance in Medicine, vol.36, 1996, p.847-857.

[28] BEHRENS T.E.J.; WOOLRICH M.W.; JENKINSON M.; JOHANSEN-BERG H.; NUNES R.G.; CLARE S.; MATTHEWS P.M.; BRADY J.M.; SMITH S.M.; *Characteriztion and propagation of uncertainty in diffusion-weighted MR imaging*, Magnetic Resonance in Medicine, vol.50, 2003, p.1077-1088.

[29] ASSAF Y.; FREIDLIN R.Z.; ROHDE G.K.; BASSER P.J.; *New modeling and experimental framework to characterize hindered and restricted water diffusion in brain white matter*, Magnetic Resonance in Medicine, vol.52, 2004, p.965-978.

[30] ZHANG H.; SCHNEIDER T.; WHEELER-KINGSHOTT C.A.; ALEXANDER D.C.; *NODDI: Practical in vivo neurite orientation dispersion and density imaging of the human brain*, NeuroImage, vol.61, 2012, p.1000-1016.

[31] WEDEEN V.J.; WANG R.P.; SCHMAHMANN J.D.; BENNER T.; TSENG W.Y.I.; DAI G.; PANDYA D.N.; HAGMANN P.; D'ARCEUIL H.; CRESPIGNY A.J.; *Diffusion spectrum magnetic resonance imaging (DSI) tractography of crossing fibers*, NeuroImage, vol.41, 2008, p.1267-1277.

[32] HESS C.P.; MUKHERJEE P.; HAN E.T.; XU D.; VIGNERON D.B.; *Q-ball reconstruction of multimodal fiber orientations using the spherical harmonic basis*, Magnetic Resonance in Medicine, vol.56, 2006, p.104-117.

[33] TUCH D.S.; *Q-ball imaging*, Magnetic Resonance in Medicine, vol.52, 2004, p.1358-1372.

[34] OZARSLAN E.; SHEPHERD T.M.; VEMURI B.C.; BLACKBAND S.J.; MARECI T.H.; *Resolution of complex tissue microarchitecture using the diffusion orientation transform (DOT)*, NeuroImage, vol.31, 2006, p.1086-1103.

[35] TOURNIER J.D.; CALAMANTE F.; GADIAN G.D.; CONNELLY A.; *Diffusion-weighted MRI fibre-tracking using a front evolution alorithm*, NeuroImage, vol.20, 2003, p.276-288.

[36] TOURNIER J.D.; CALAMANTE F.; GADIAN G.D.; CONNELLY A.; *Direct estimation of the fiber orientation density function from diffusion-weighted MRI data using spherical deconvolution*, NeuroImage, vol.23, 2004, p.1176-1185.

[37] TOURNIER J.D.; CALAMANTE F.; GADIAN G.D.; CONNELLY A.; *Improved probabilistic streamlines tractography by 2nd order integration over fibre orientation distributions*, Proc. Intl. Soc. Mag. Reson. Med. (ISMRM), vol.18, 2010, p.1670.

[38] AURIAT A.M.; BORICH M.R.; SNOW N.J.; WADDEN K.P.; BOYD L.A.; *Comparing a diffusion tensor and non-tensor approach to white matter fiber tractography in chronic stroke*, vol.7, 2015, p.771-781.

[39] SONG F.; HOU Y.; SUN G.; CHEN X.; XU B.; HUANG J.H.; ZHANG J.; *In vivo visualization of the facial nerve in patients with acoustic neuroma using diffusion tensor imaging-based fiber tracking*, Journal of Neurosurgery, vol.125, 2016, p.787-794.

[40] YOSHINO M.; KIN T.; ITO A.; SAITO T.; NAKAGAWA D.; INO K.; KAMADA K.; MORI H.; KUNIMATSU A.; NAKATOMI H.; OYAMA H.; SAITO N.; *Feasibility of diffusion tensor tractography for preoperative prediction of the location of the facial and vestibulocochlear nerves in relation to vestibular schwannoma*, Acta Neurochirurgica, vol.157, 2015, p.939-946.

[41] FARQUHARSON S.; TOURNIER J.D.; CALAMANTE F.; FABINYI G.; SCHNEIDER-KOLSKY M.; JACKSON G.D.; CONNELLY A.; *White matter fiber tractography: why we need to move beyond DTI*, Journal of Neurosurgery, vol.118, 2013, p.1367-1377.

[42] "NIFTI-1 Data Format". October 2007. https://nifti.nimh.nih.gov/nifti-1/

[43] "dcm2niix". *github*. https://github.com/rordenlab/dcm2niix

[44] ANDERSSON J.L.R.; SOTIROPOULOS S.N.; *An integrated approach to correction for off.resonance effects and subject movement in diffusion MR imaging*, NeuroImage, vol.125, 2016, p.1063-1078.

[45] WEISSKOFF R.M.; DAVIS T.L.; *Correcting gross distortion on echo planar images*, Proceedings of the SMRM $11^{th}$ Annual Meeting.

[46] JEZZARD P.; BALABAN R.S.; *Correction for geometrical distortion in echo planar images from bo field variations*, Magnetic Resonance in Medicine, vol.34, 1995, p.65-73.

[47] CHEN N.K.; WYRWICZ A.M.; *Optimized distortion correction technique for echo planar imaging*, Magnetic Resonance in Medicine, vol.45, 2001, p.525-528.

[48] CHEN N.K.; WYRWICZ A.M.; *Correction for epi distortions using multi-echo gradient-echo imaging*, Magnetic Resonance in Medicine, vol.41, 1999, p.1206-1213.

[49] KYBIC J.; THEVENAZ P.; NIRKKO A.; UNSER M.; *Unwarping of unidirectionally distorted epi images*, IEEE Transactions on Medical Imaging, vol.19, 2000, p.80-93.

[50] STUDHOLME C.; CONSTABLE R.T.; DUNCAN J.S.; *Accurate alignment of functional epi data to anatomical mri using a physics-based distortion model*, IEEE Transactions on Medical Imaging, vol.19, 2000, p.1115-1127.

[51] ANDERSSON J.L.R.; SKARE S.; ASHBUMER J.; *How to correct susceptibility distortions in spin-echo echo-planar images: application to diffusion tensor imaging*, NeuroImage, vol.20, 2003, p.870-888.

[52] LE BIHAN D.; POUPON C.; AMADON A.; LETHIMONNIER F.; *Artifacts and Pitfalls in Diffusion MRI*, Journal of Magnetic Resonance Imaging, vol.24, 2006, p.478-488.

[53] HOTELLING G.; *Analysis of a complex of statistical variables into principal components*, Journal of educational psychology, vol.24, 1933.

[54] VERAART J.; NOVIKOV D.S.; CHRISTIAENS D.; ADES-ARON B.; SIJBERS J.; FIEREMANS E.; *Denoising of diffusion MRI using random matrix theory*, NeuroImage, vol.142, 2016, p.394-406.

[55] *FSL*. 25-11-2017. https://fsl.fmrib.ox.ac.uk/fsl/fslwiki

[56] *MRtrix3*. https://mrtrix.readthedocs.io/en/latest/index.html

[57] *ANTs*. http://stnava.github.io/ANTs

[58] *MathWorks*. 1994-2018. https://it.mathworks.com/products/matlab.html

[59] TOURNIER J.D.; CALAMANTE F.; CONNELLY A.; *MRtrix: Diffusion tractography in crossing fiber regions*, Int. J. Imaging Syst. Technol., vol.22, 2012, 53-66.

[60] *ITK-SNAP*. http://www.itksnap.org/pmwiki/pmwiki.php

[61] *FarmacoeCura.* 2018. https://www.farmacoecura.it/wp-content/uploads/2010/05/Nervo-facciale.png

[62] SAMPATH P.; RINI D.; LONG D.M.; *Microanatomical variations in the cerebellopontine angle associated with vestibular schwannomas (acoustic neuromas): a retrospective study of 1006 consecutive cases*, Journal of Neurosurgey, vol.92, 2000, p.70-78.

[63] KOOS W.T.; DAY J.D.; MATULA C.; LEVY D.I.; *Neurotopographic considerations in the microsurgical treatment of small acoustic neurinomas*, Journal of Neurosurgey, vol.88, 1998, p.506-512.

# ACKNOWLEDGMENT

I would first like to thank my thesis supervisor professor Alessandra Bertoldo, for giving me the opportunity to do this work. I would also like to acknowledge my co-supervisors Sabrina and Marco for being there whenever I ran into a trouble spot or had a question about my research or writing. They steered me in the right direction whenever I needed it and I am gratefully indebted to them for the very valuable comments on this thesis.
I would also like to thank the experts who were involved in the validation survey for this research project: the neuroradiologist Mariagiulia Anglani, the neurosurgeons Valentina Baro and Andrea Landi and the otolaryngologist Elisabetta Zanoletti. Without their passionate participation and input, the validation survey could not have been successfully conducted.
I must express my very profound gratitude to my parents and to my sister for their continuous encouragement and for the financial support. Together with them I would also like to thank all my family, including uncles and cousins, and Andrea's family, who have been of moral support in these years even if they do not know it.
To Cristina, Erika, Gaia, Irene, Marta, Noemi and Stefania: thank you, each of you knows what we have shared together .
I would also like to thank the people I met during these university years, especially Giulia C., Giulia N., Jessica and my sincere, precious and irreplaceable friend Francesca.
Finally, my most heartfelt thanks go to Andrea, to whom I dedicate this thesis, for providing me with unfailing support and constant encouragement throughout these six years. This accomplishment would not have been possible without him. Thank you.

Manuela Moretto